TECHNISCHE UNIVERSITÄT WIEN
Vienna University of Technology

ACIN
AUTOMATION & CONTROL INSTITUTE
INSTITUT FÜR AUTOMATISIERUNGS- & REGELUNGSTECHNIK

Development of Compact, Long-Range Atomic Force Microscope for In-Line Measurements

DIPLOMARBEIT

Ausgeführt zum Zwecke der Erlangung des akademischen Grades eines
Diplom-Ingenieurs (Dipl.-Ing.)

unter der Leitung von

Univ.-Prof. Dr.sc.techn. Georg Schitter
Univ.Ass. Dipl.-Ing. Poik Mathias BSc

eingereicht an der
Technischen Universität Wien
Fakultät für Elektrotechnik und Informationstechnik
Institut für Automatisierungs- und Regelungstechnik

von

Mario Mayr, BSc
Matrikelnummer: 1526414

Wien, im Jänner 2022

Advanced Mechatronic Systems Group
Gußhausstraße 27-29, A-1040 Wien, Internet: http://www.acin.tuwien.ac.at

Danksagung

An erster Stelle gilt mein besonderer Dank meinem Betreuer Mathias Poik, der mir geduldig und unermüdlich mit Rat und Tat zur Seite stand. Ich möchte mich auch bei Prof. Georg Schitter und seinem Team (Advanced Mechatronics Systems group) für das herausragende Arbeits- und Forschungsumfeld bedanken. Besonderer Dank gilt Thomas Hackl und Daniel Wertjanz für wertvolle Tips bei der praktischen Umsetzung. Ich möchte mich bei alle meinen Freunde und Kollegen an der Universität für eine unvergessliche Zeit bedanken.
Abschließend möchte ich meiner ganzen Familie insbesondere meinen Eltern Robert und Regina, und meiner Freundin Julia herzlich bedanken denn ihr habt mich mein ganzes Leben lang unterstützt und motiviert und dadurch diese Arbeit erst ermöglicht.

Vielen Dank!

Abstract

The Atomic force Microscope (AFM) is a powerful tool for the analysis of surface topography and various properties like roughness on atomic scales and up to μm structures. It uses a sharp tip, which is scanned over the investigated surface, while the tip-surface force is usually kept constant in a feedback loop. The tip motion requires (sub-)nanometer accuracy, and AFMs are sensitive to floor vibrations. AFMs are therefore typically operated in quiet laboratories with remedies against floor vibrations.

With growing demand for products fabricated in the nanoscale the necessity of in-line measurement tools with high resolution arises and the AFM is one of the most versatile measuring tools at the nanoscale. For AFM measurements in harsh environmental conditions, such as industrial production lines, active vibration compensation measures have to be applied. Additionally, the AFM measurement head requires a compact size and a long vertical stroke to enable high bandwidth tracking of floor vibrations with large amplitudes (>10 μm).

In this project, a compact, long-range AFM with vibration sensors on 3 axes for in-line measurements is developed. The impact of floor vibrations on the AFM imaging performance is analyzed. Based on the analysis, a suitable mechanical setup is designed and simulated. In order to enable large area-analysis a long range scanner is designed. The performance of the developed AFM is evaluated on test samples subjected to floor vibrations and test vibration profiles.

A flexible and compact AFM with piezoresistive deflection measurement is designed, simulated and evaluated. The AFM is just 16 x 16 x 12 cm and weighs 1.5kg. The AFM is capable of scanning 220 x 220 μm at a line scan rate of 1 Hz, respectively 340 x 340 μm at 0.5 Hz while the scanner is operated open loop with a linearty error below 0.5%. The presented concept is able to reject a out-of-plane disturbance with 5 Hz and 500 nm peak-peak with 40 dB. Further it is shown that it is possible to take AFM topography images while the sample is exposed to vibrations that would damage the tip, cantilever or both with out remedies against vibrations. In-plane vibrations up to 1.5 μm are well corrected by the presented offline trajectory error correction method. Both methods still work if the sample is vibrating in-plane and out-of-plane simultaneously.

Zusammenfassung

Das Rasterkraftmikroskop (AFM) ist ein leistungsfähiges Werkzeug für die Analyse von Oberflächentopografien und verschiedener Oberflächeneigenschaften wie z.B. Rauheit auf atomarer Ebene und bis zu μm großen Strukturen. Es verwendet eine scharfe Spitze, die über die untersuchte Oberfläche gescannt wird, wobei die Kraft zwischen Spitze und Oberfläche in der Regel in einer Rückkopplungsschleife konstant gehalten wird. Die Bewegung der Spitze erfordert eine Genauigkeit im (Sub-)Nanometerbereich, und AFMs sind empfindlich gegenüber Bodenvibrationen. AFMs werden daher in der Regel in vibrationsaremen Labors mit speziellen Maßnahmen gegen Bodenvibrationen betrieben.

Mit der wachsenden Nachfrage nach Produkten, die im Nanometerbereich hergestellt werden, entsteht die Notwendigkeit eines Inline-Messgerats mit hoher Auflösung, und das AFM ist eines der vielseitigsten Messgeräte im Nanometerbereich. Für AFM-Messungen in harschen Umgebungen, wie z.B. in industriellen Produktionslinien, müssen aktive Vibrationskompensationsmaßnahmen angewendet werden. Daŕuber hinaus benötigt der AFM-Messkopf eine kompakte Größe und einen langen vertikalen Hub, um Bodenvibrationen mit großen Amplituden (>10 μm) mit hoher Bandbreite ausgleichen zu können.

In diesem Projekt wird ein kompaktes AFM mit großer Reichweite und Vibrationssensoren auf 3 Achsen für Inline-Messungen entwickelt. Der Einfluss von Bodenvibrationen auf die AFM-Bildqualität wird analysiert. Basierend auf der Analyse wird ein geeigneter mechanischer Aufbau entworfen und simuliert. Um eine großflachige Analyse zu ermöglichen, wird ein Long-Range-Scanner entwickelt. Die Leistungsfähigkeit des entwickelten AFMs wird an Testproben, die Bodenvibrationen und Testvibrationsprofilen ausgesetzt sind evaluiert.

Ein flexibles, kompaktes, auf piezoresistiver Cantilever basierendes AFM wird entworfen, simuliert und evaluiert. Das AFM ist nur 16 x 16 x 12 cm groß und wiegt 1.5 kg. Das AFM ist in der Lage, 220 x 220 μm bei einer Linenscanrate von 1 Hz bzw. 340 x 340 μm bei 0.5 Hz zu scannen, während der Scanner im offenen Regelkreis mit einem Linearitätsfehler unter 0.5% betrieben wird. Das vorgestellte Konzept ist in der Lage, eine Störung außerhalb der Ebene bei 5 Hz und 500 nm Spitze-Spitze mit

40 dB zu unterdrücken. Weiterhin wird gezeigt, dass es möglich ist, AFM-Topographie-Bilder aufzunehmen, während die Probe Vibrationen ausgesetzt ist, die die Spitze, den Cantilever oder beide beschädigen würden. Vibrationen in der Ebene mit 1.5 μm werden durch die vorgestellte Nachbearbeitung zur Korrektur von Trajektorienfehlern gut korrigiert. Beide Methoden funktionieren auch, wenn die Probe gleichzeitig in der Ebene und außerhalb der Ebene schwingt.

Contents

List of Figures

CHAPTER 1

Introduction

1.1 Background and Motivation

The Atomic Force Microscope (AFM) is a high resolution scanning probe microscope and is applied in a wide range of natural sciences such as semiconductor engineering [1, 2], solid-state physics [3], molecular engineering [4], polymer and surface chemistry [5], biology and medicine [6, 7]. It is one of the most versatile tools for imaging, measuring, and manipulating at the nanoscale. It is capable of topography imaging with sub nanometer resolution [3]. AFMs offer a high resolution over a large range [8]. There are many different measurement modes which are suitable for determining properties of the sample beyond topography measurements. Some examples are Kelvin Probe Force Microscopy for measuring contact potential differences [9], investigating the inter molecular forces on the nanoscale in live sciences [10] or Magnetic Force Microscopy [11]. Imaging in air, liquids [12] as well as vacuum [13] is possible.

The AFM [14] uses a sharp tip fabricated at the end of a cantilever to measure surface properties. Tip and sample are brought into contact and the tip is scanned over the investigated sample surface. The force between tip and sample leads to a deflection of the cantilever. The force is determined by measuring the deflection of the cantilever. Figure 1.1 shows a two dimensional illustration of the working principle of an AFM with the most important parts. The most common way of deflection measurement in AFMs is a laser beam which reflection angle is depending on the deflection. With changing the reflection angle the position of the laser beam on the 4 quadrant photo detector is changing and the deflection is read out [15]. An alternative but less common way of deflection measurement are cantilevers with piezoresistive elements fabricated to the base of the cantilever beam. When the deflection of the piezoresistive cantilever changes the resistances of the piezoresistive elements changes proportionally. This change in resistance can be measured with e.g. a bridge circuit [16]. While scanning the tip-surface force is usually kept constant by adjusting the vertical tip-surface distance in a feedback loop. The controller output is proportional to the sample topography. In a more mathematical way the tip and the sample perform a convolution resulting in

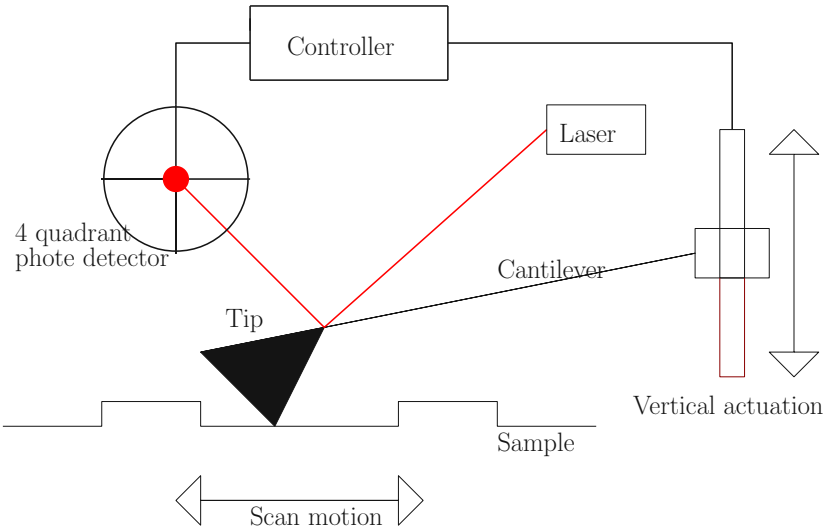

Figure 1.1: Two dimensional AFM working principle with laser-photo detector deflection measurement.

a topography image [17]. The sample has to be positioned sufficiently perpendicular to the vertical axis otherwise the sample tilt in combination with the limited vertical range limits the scan range. In opposite to optical methods such as scanning confocal chromatic sensors [18] the sample has to be sufficiently flat in order to prevent tip and the cantilever from damage. Depending on the tip size the height of sharp edges of the sample features should usually not be higher than several μm [19]. There are no further typical requirements for the sample and its preparation [20]. For example the sample does not have to be conductive, as in scanning electron microscopy and transmission electron microscopy [21].

AFMs are obviously a very powerful tool and they could be used in production process lines to give insights to the processes. With growing demand for products fabricated in the nanoscale [22] such as Central Processing Units (CPUs) [23], Graphic Processing Units (GPUs) [24] and power electronics [25, 26], the necessity to monitor these production processes with high resolution occurs. In future production lines in-line measurement will become more important and will become a key technology [27, 28]. As in-line quality control tool or process monitoring device e.g. surface roughness correlates with tool wear [29, 30]. There is an example where AFM is used as in-line quality control and correction tool. In this case the AFM is used after a production step for fast defect detection and repairing of high resolution photomasks [31]. AFMs are currently not broadly used in-line, because vibrations are not distinguishable from the sample topography in commercial AFMs [32] and vibrations are usually omnipresent in industrial environment [33].

1.2 Problem description

AFMs are sensitive to vibrations between the tip and the sample [34, 32]. These vibrations can be induced by people, traffic [19, 35], construction work [36] or appliances [37]. AFMs are therefore usually operated in laboratory environments on decoupled tables

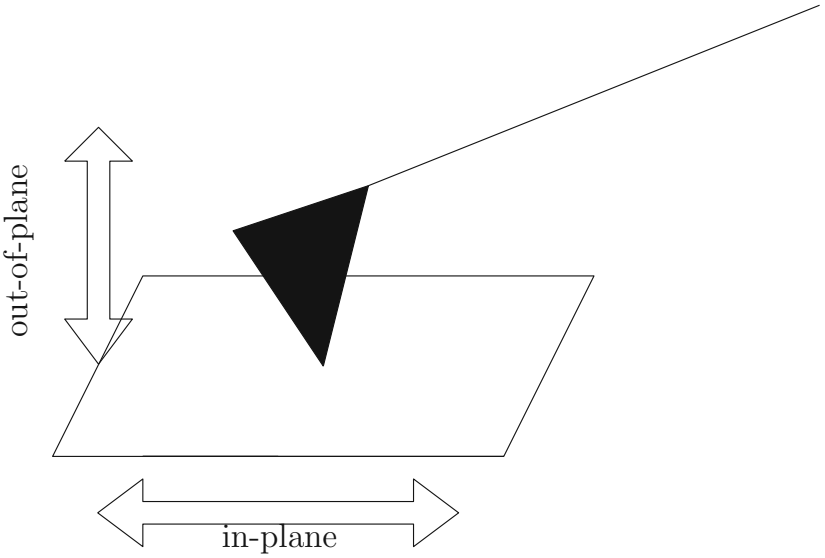

Figure 1.2: Visualization of the vibration directions, in-plane and out-of-plane relative to the plane defined by the sample.

with high mass for vibration rejection [38]. AFM cantilevers are very fragile therefore the tip has to be positioned precisely on the sample. This requires precise actuation for the tip sample engage process. The main obstacle for in-line AFM imaging are the tip-sample vibrations, since production lines are typically harsh environments with strong vibrations [33]. AFMs are usually bulky devices which limits their usability in confined spaces. Furthermore AFMs are typically heavy setups with several kg and are therefor difficult to move and position with e.g. a robot or spindle. Typically commercial AFMs have a limited scan range of approximately 100 μm. A higher scan range can be of advantage for in-line use as it enable the examination of a larger area in a single scan. Another challenge for in-line measurements is often the required throughput limited by the measurement duration and sample loading time [39]. With out any remedies against vibrations, displacements in all spatial directions must be expected. In this thesis a differentiation between in-plane and out-of-plane is made. A visualization of the vibration directions is shown in Figure 1.2. Out-of-plane means vibrations perpendicular to the plane defined by the sample. In-plane means vibrations parallel to the sample plane. Out-of-plane vibrations are not distinguishable from the sample topography in commercial AFMs, with just a cantilever as vertical sensor.[32]. There is literature discussing the influence of these vibrations and remedies against them, which are presented in detail in the State of the Art chapter. To the knowledge of the author there is no literature explicitly discussing in-plane disturbances. The in-plane movement of the sample poses a disturbance to the scan trajectory, this results in a height signal measured at the wrong position and consequently leads to a disturbed topography image.

1.3 Aim

An AFM for in-line must have remedies against tip-sample vibration, it should be compact and have a long range on the out-of-plane axis in order to deal with imprecise positioned and tilted samples. Moreover a long scan range is an advantage as it enables the analysis of a large areas in single scan. The aim of this thesis is to design, simulate and evaluate a flexible, light weight and compact AFM prototype with a large scan range and with remedies against out-of-plane and in-plane vibrations. This prototype should bring the AFM one step closer to be broadly usable for in-line metrology.

1.4 Overview

The thesis starts with Chapter 2(**State of the Art**), where common vibration profiles in industrial and urban environments are presented, further research on active vibration rejection on AFMs is discussed.
The Chapter 3(**System Design and Simulation**) presents a concept for a long range scanner and a scan head with additional vibration sensors. The vertical actuation and an assembly of the whole system is presented and for critical parts a simulations are discussed.
In Chapter 4(**Evaluation**) the different parts of the system are evaluated with measurements and experiments. The chapter is finished by AFM images measured by the built system and a high bandwidth controller design for the vertical axis.
Since it is proven that the AFM works in the previous chapter it is now time to analyze the performance of the setup subjected to vibrations in Chapter 5(**Experiments with Vibrating Sample**).
The second experimental Chapter 6(**Long Range Experiments**) shows the long range capabilities of the built AFM.
The thesis is recapitulated in Chapter 7(**Conclusion**) and an outlook is given.

CHAPTER 2

State of the Art

In order to design a compact long range in-line AFM related work is analyzed. Typically AFMs are used in a laboratory environment on vibration isolating tables. However, for in-line measurements tip sample vibrations are expected. The amplitudes and frequencies of these vibrations are discussed first, followed by a discussion of active vibration rejection for AFMs and their capabilities for in-line measurements. To design a compact long range AFM examples of compact and long range AFM designs are discussed. Further metrological AFMs are discussed. A discussion regarding in-plane displacement sensors and their limitations is presented. For better understanding the advantages and drawbacks of the two most common AFM measurement modes are presented.

2.1 Typical Vibrations

Vibrations are basically everywhere. In this section their sources and characteristics are discussed. Traffic induced vibrations in buildings are excited predominately in low frequencies of around 0.5- to 10 Hz. Their maximum displacement and the exact frequency distribution is depending on the height of the building. Vibration amplitudes of several μm can be expected [19].
Production steps like milling and the necessary industrial appliances are causing vibrations. In [40] the vibrations of a 6 degree of freedom robot with a mill are analyzed in order to design a optimal feedback controller. It is found that the robot-mill assembly showed several structural modes with eigenfrequencies of several 10 Hz. With feedback control applied vibration amplitudes up to 100 μm are measured.
Construction work is a also a common source of vibrations. As an example sheetpile driving causes vibrations with 20 μm amplitude at 11 m distance form the construction site, with typical frequencies of several 10 Hz [36].
In [33] vibrations measured at a work piece support table at a micro and nano coating manufacturer are analyzed. It is found that the continuously present vibrations are

caused by e.g. production machines cause continuous vibrations that have a peak-peak value of 400nm. Significant vibration peaks at 25, 50 and 100 Hz are observed. Further impulses with an amplitude of 6 μm are measured caused by operating personal and other non periodic events .

The discussed vibrations with several 10 Hz and amplitudes in the μm will definitely disturb the AFM measurements without further remedies. Some of the high amplitude vibrations like due to construction work might damage the AFM. The vibration rejecting remedies must compensate these high amplitude peak vibrations good enough to prevent the instrument from damage and should reject continues vibrations in way that the required image resolution is reached [33]. Remedies against the discussed vibrations are presented in next section

2.2 Vibration Rejecting AFMs

In [32] an AFM with a distance sensor in addition to the cantilever is implemented, the AFM is operated as differential measurement device. A additional capacitve distance sensor is attached to the AFM head to measure the vibrations. The measured vibrations during scanning are subtracted from the measured topography obtained by the controller output in a post processing step. The sample was vibrating sinusoidal with 10 Hz and 100 nm peak-peak. The offline subtraction of the measured disturbance resulted in an disturbance free topography image. The sample is only vibrating out-of-plane.
In [34] a two stage actuation for long range vertical disturbance rejection is designed. A vertically moving platform with long range actuators is implemented and the distance from the moving platform to the sample is measured by a position sensor. For the long range action four Lorentz actuators are selected, and the control loop is specifically designed for vibration rejection and isolation. The whole AFM head is installed on the moving platform. This means the short range actuator is the vertical piezo of the AFM head, and the AFM is operated in constant force mode with a second feedback loop. This enables AFM imaging on sample which are vibrating out-of-plane. Floor vibrations are reduced from 358 nm rms to 2.48 nm rms, which is a disturbance rejection of -43.2 dB. The sample is moved during scanning not the whole vertical setup, this is not possible in many in-line situations.
In [41, 42, 43] several measurement principles with the capability of measuring in the nanometer range are installed on a measurement platform mounted to a industrial robot and enabling in-line nanometrology measurements are analyzed. An AFM is mounted to a 6 degree of freedom vibration rejection platform which is mounted on the endeffector of an industrial robot. Using position measurement with 6 position sensors and additional targets for the in-plane measurement and a feedback control with 6 individually adjustable single-input single-output controllers. The platform can follow the motion of the target with a remaining position error of 22, 17 and 14 nm in x-, y- and z-direction. This approach improves the positioning accuracy by three orders of magnitude compared to conventional industrial robots with position error in the range of several 10 μm. A compact AFM with piezo resistive strain gauges as deflection measurement is designed. The AFM scanner had a range of 100 x 100 μm.

In [32] the disturbance rejection for 100 nm peak peak is verified which is a too small range for the typical vibrations in production lines e.g. semiconductor fabrication [33], the setup in [34] is verified up to vibrations with 2 μm but the assembly is heavy and large and therefore difficult to move and position with e.g. a robot or spindle. In [41, 42, 43] AFM imaging is enabled on a 6 degree of freedom industrial robot with a vibration rejection platform with 20 nm position error. The AFM mounted to the platform uses piezoresistive elements for deflection measurement. No further details of the AFM setup are published. The idea of using piezorestive elements to design a compact and light AFM is further discussed later on in the next section. Non of the discussed papers are explicitly discussing in-plane vibrations in detail.

2.3 Compact AFM-setups and Piezoresistive Cantilevers

To enable robot based in-line measurements like in [41] the measurement system is preferably light and compact. In general light and compact designs lead to flexible measurement devices for in-line measurements [28]. The laser-photo detector deflection measurement setup with the required optical path leads to bulky and heavy AFM setups. A more compact and lighter alternative is piezoresistive defection measurement. A typical way of fabrication for such piezoresistive cantilevers is a p-type resistor which is fabricated at the surface of the cantilever so that the piezoresistive effect of silicon causes its resistance to vary linearly with its deflection. The design and fabrication of cantilevers with piezoresistive elements for deflection measurement is presented in [16]. Moreover the working principle of these cantilevers is verified by using them for AFM imaging.
Figure 2.1 shows a common way to measure the resistance change proportional to the deflection. The change in resistance is measured with bridge circuits usually with differential instrumentation amplifiers for the bridge output voltage. The output voltage of the circuit is proportional to deflection of the cantilever. Further the bridge circuit in combination with the piezoresistive cantilever offers a efficient solution for deflection amplitude measurement for tapping mode imaging [44, 45].
The deflection measurement is done with piezorestive cantilever in [46] resulting in a light and compact AFM system, which possesses the capability of rapid and large area surface topography measurement. In [41] a similar approach for the compact and light weight AFM setup is used.
A single chip MEMS(Micro-Electro-Mechanical System)-based AFM with an additional vertical long range actuation and a scan range of 30 x 12 μm is presented in [47]. The deflection measurement was done via piezoresistive elements. A line scan rate of 41Hz is achieved for a scan range of 8 x 8 μm. As long range actuator a flexure guided voice coil actuator is used. The whole system is designed for in-line wafer probing, measuring nanoscale features in semiconductor manufacturing systems, but the influence of external vibrations is not discussed.
Literature show that the use of cantilevers with piezoresitve elements results is compact and fast AFM setups [47, 46]. It is proven that compact setups with piezoresistive

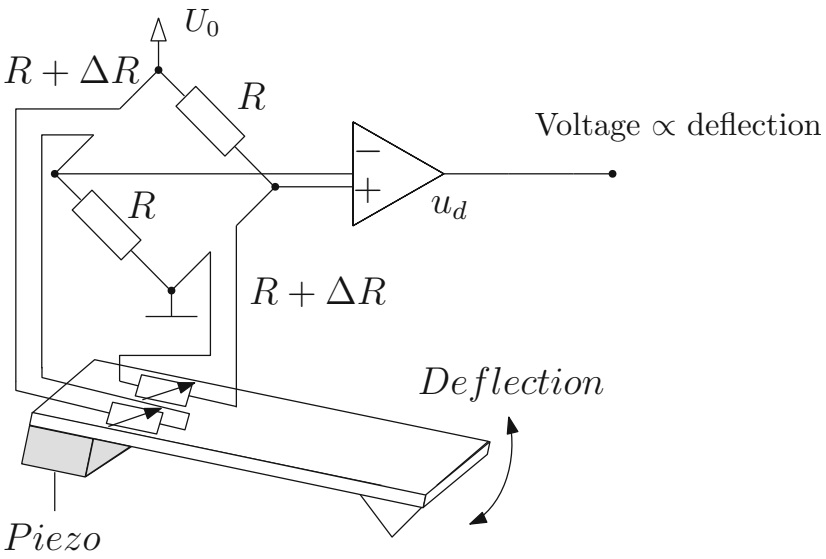

Figure 2.1: Piezoresistive deflection measurement witth half bridge cicruit. The piezoresistive elements are at the base of the cantilever, and a differential amplifier is amplifying the bridge output voltage, inspired by [44].

cantilevers are capable of robot based in-line measurements in combination with a vibration rejecting platforms in [41]. The in this section discussed setups all have a scan rang of 100 μm or less. The next section examines work regarding long range AFM setups.

2.4 Long Range AFM

A long stroke scanner for an AFM for the Dutch standards laboratory is presented in [48]. This instrument consists of a scanner stage with a range of 1 x 1 x 1 mm and a custom built AFM head. The design of the translation stage, consisting of flexures, Lorentz actuators with weight and stiffness compensation for power loss reduction and interferometric translation measurement is presented. The stage is used for translating the sample vertically while the AFM head remains stationary. The approach of moving the sample and mounting the AFM head at fixed position is also used for high speed imaging in [49, 50].
A typical trade-off for AFM designs is between range and controller bandwidth. Usually a long range on the vertical axis leads to a low controller bandwidth. The limitation of the bandwidth range product which is describing the trade-off limitation is broken in [51]. An AFM with a flexure guided voice coil actuator that vertically moves a piezoresistive cantilever is built. The second resonance frequency of the setup is maximized for a high control bandwidth while the first resonant frequency is relatively low due to the low stiffness required for the range. A control bandwidth of 881Hz is achieved for 700 μm vertical range with a resolution of 1.7 nm. Moreover the high controller bandwidth leads to a good disturbance rejection. In this work the sample is moved by an external scanner.
The discussed papers [51, 48] in combination with [34] suggest that Lorentz-actuators

are the best actuation solution for long range AFM imaging. For long range and high speed scanning the approach of moving the sample instead of the whole AFM head is often used like in [49, 50, 48] since the sample is much lighter than the AFM head. This approach is not possible in every in-line situation. The approach of measuring the movement of the sample in [48] is presented in detail in the next section.

2.5 Metrological AFM

Most commercial AFMs have significant measurement uncertainties due to thermal drift and limited repeatability. Metrological AFMs, on the other hand, have a frame of interferometers as a metrology system. Since the wavelength of a laser source is related to the definition of the meter, these devices are able to produce measurements directly traceable to the length standard [52]. This measurement frame covers the out-of-plane axis and both in-plane axes. Metrological AFMs are used where the traceability to the definition of the meter is necessary [53, 52]. Usually national metrology standard institutions like e.g. french Laboratoire National de metrologie et d'Essais with their metrological AFM described in [54] and the Dutch standards laboratory [48] use them. In [52] the design of a metrological AFM is presented, with the focus on the sample approach mechanism. The instrument consist of three frames, a metrology frame, a positioning frame and a base frame supporting the other two frames. In order to increase the thermal stability of the measurement loop, the metrology frame is made out of invar, an iron-nickel alloy with a very low coefficient of thermal expansion, while the rest is made out of aluminum. Since the thermal vibrations are measured by the interferometers anyway invar is not necessary on the other frames. The instruments are operated on vibration isolation tables and their structures are high stiffness designs in favor of reduced sensitivity to vibrations [54, 52].
Due to their complex structure and the required laser source the setups discussed in [53, 54, 52, 48] become very large and heavy. Typically fast and easy sample loading is not possible in this complex assemblies as described in [52], this prevents them from being usable in-line apart from their high costs. The idea of measuring the in-plane sample position relative to the tip is further discussed in Chapter 3 in the concept part and the next section.

2.6 In-plane Sensors

The in the previous section described metrological AFMs use interferometers to determine the exact sample position. The interferometers offer a high resolution over a large range but require reflective targets and precise leaser beam alignment on all axes. All of this is unfavorable for in-line use.
An advantage of laser speckle based in-plane measurement methods [55] would be that no additional markers are required. But the target surface has to be optically rough [56]. Markers are not favored in in-line metrology [57]. In [57] a compensation based laser sensor system capable of measuring in-plane as well as out-of-plane displacements of a target is presented. The out-of-plane distance is measured by laser triangulation while

the in-plane measurement is based on objective laser speckle measurement. Both measurement methods are integrated into one sensor device. An in-plane and out-of-plane resolution of 3 μm and 1 μm respectively is achieved.
In [58] a commercially available laser speckle based mouse senor is analyzed. A custom build readout box is build and presented. The sensor is compact and light with dimensions of 27 x 22 mm. A resolution of 12000 dpi is achieved, which corresponds to 2.12 μm.
An alternative would be two-dimensional position sensitive photo-detectors [59]. A commercially available example would be (First Sensor, Berlin, Germany) PSD DL100-7 THD with a resolution limit of 0.2 μm due to noise. Large area position sensitive photo-detectors with a better resolution are part of current research e.g. a resolution of 100 nm is reached in [60]. The drawback of these method is that a LED or laser marker near the sample is necessary.

2.7 AFM Measurement Modes

Contact Mode: As described in Chapter 1.1, a feedback controller keeps the force between tip and sample constant. Contact mode with constant force is a very simple and common operational mode for AFMs. Its main drawback are strong tip sample interactions which can lead to sample damage and imaging artifacts at high tip speeds [61]
Tapping Mode: Amplitude modulation AFM usually called tapping-mode is the most common modulating measurement method [62]. The AFM cantilever is excited close to its mechanical resonance frequency and the interaction forces between tip and sample lead to a modulation, i.e. a frequency variation of amplitude and phase shift, of the cantilever oscillation. Tapping mode utilizes the oscillation amplitude for feedback control to obtain the surface topography. Simultaneously, the phase can be recorded providing information about local mechanical properties [44]. Compared to contact mode the tip sample interactions are reduced and sample damage in flat surfaces like silica is not observed in [61].
Since this work focuses on vibration rejection for in-line measurement contact mode is implemented, the setup is designed in a way that the implementation of tapping mode will also be possible for further work on this setup.

CHAPTER 3

System Design and Simulation

Based on the insights regarding vibration profiles, long range AFM setups, compact AFM designs and requirements for in-line measurements discussed in the previous Chapter 1 and Chapter 2 a concept for an in-line AFM is presented in this chapter. At first the general concept is outlined then out-of-plane and in-plane vibration rejection concept are discussed in detail. With a defined concept specific actuators and sensors are selected. Later on requirements for the setup are defined and with this requirements calculations for unknown parameters are carried out. An assembly of the proposed setup is presented. For critical parts of the setup simulations are carried out.

3.1 Concept

The goal is to design an AFM capable of long range in-line topography measurements. To perform topography measurements vertical and lateral actuation is required. As discussed in Chapter 2.1 vibrations are omnipresent in industrial environments without isolating tables therefore an AFM used in-line must have remedies against vibrations in-plane and out-of-plane.
Figure 3.1 shows the outline of the proposed concept. A compact AFM head is designed which holds a cantilever, an additional out-of-plane distance sensor and a sensor for in-plane distance measurements. The AFM head is placed over the sample. The sample is not moved in this work since it is not possible in many in-line measurement situations. Therefore, the AFM head has to be actuated for vertical motion and scanning. A cantilever with piezoresistive elements for deflection measurement is used. For topography measurements in contact mode a feedback controller is a applied for the vertical axis. As actuation principle for all axes Lorentz actuators driven by a current controller are selected. The details for the out-of-plane and in-plane vibration rejection are discussed in the following two sections.

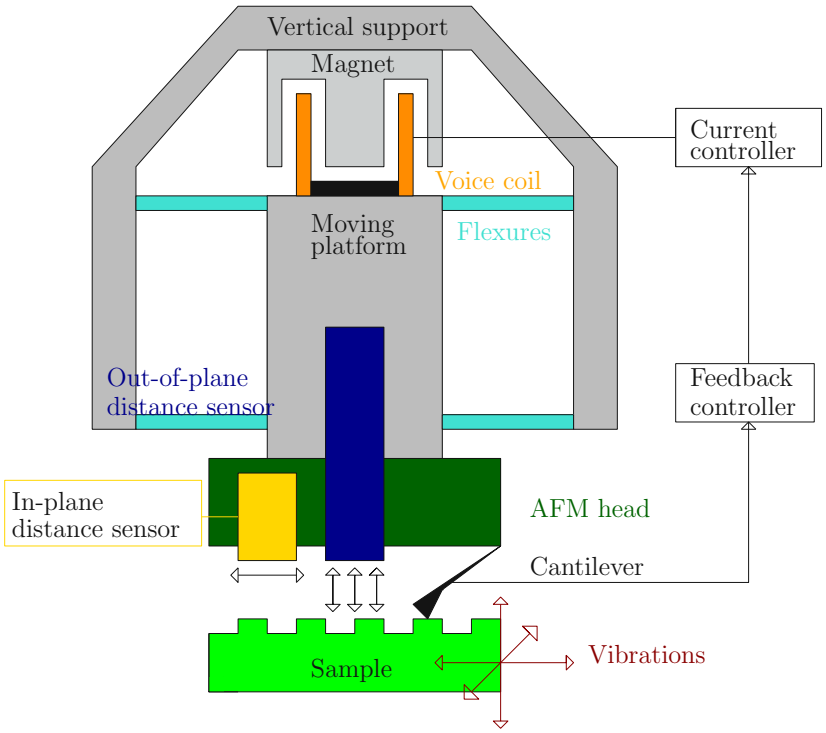

Figure 3.1: Concept for the vertical actuation and the sensor placement. In bright green is the vibrating sample. The dark green AFM head holds the in-plane-distance sensor, in yellow and the additional out-of-plane distance sensor in dark blue. The moving part is guided by flexures fixed to the vertical support frame. The magnet of the voice coil actuator is mounted to vertical support frame. The voice coil in orange is driven by a current controller. The feedback loop is using the cantilever as sensor.

3.1.1 Out-of-plane with Vibration Compensation

For the vibration rejection of the vertical axis respectively the out-of-plane vibrations a second distance senor additionally to the cantilever is used in [32] and the measured disturbance is subtracted from the controller output in a post processing step. The concept here is similar to [32] except that no post processing is necessary. An overview of the concept for the vertical axis is given in Figure 3.1. There is also a second distance sensor in addition to the cantilever, like in [32] on the AFM head. The additional sensor measures the average distance in a larger area. The control loop is operated using the cantilever as sensor, the output of the controller is proportional to the vibrations and the sample topography. Since the feedback loop keeps the force between tip and sample constant and therefore also the distance between tip and sample constant the AFM head is vertically moving in the same way as the sample. The second vertical distance sensor which is mounted to the AFM head is therefore measuring the height change due to the sample topography, assuming a ideal control loop. Practically the performance of the control loop is influencing the vibration rejection. In order to receive a compact and flexible setup a single stage actuation is used on the vertical axis. In [51] it is shown that flexure guided voice coil actuators enable vertical long

range imaging with a high resolution and high controller bandwidth. A long range AFM setup with Lorentz actuators is presented in [48]. As suggested by literature a flexure guided Lorentz actuator in form of a voice coil actuator with a low noise current controller is selected as actuation concept due to the high achievable range. The vertical part is specifically designed to reject tilt modes by having flexures on the upper and the lower part of the moving platform. It is shown in [41] that AFM designs with piezoresitive deflection measurement are capable of in-line measuring in combination with a vibration rejecting platform. In [46] a compact high speed AFM based on piezoresistive deflection measurement is presented. In [51] the advantages of piezoresistive deflection measurement concerning low mass are discussed and it is shown that the low mass of piezoresistive deflection measurement allows high controller bandwidth combined with high ranges. As motivated in Chapter 2.3 the deflection is measured with piezoresitive elements in order to design a compact AFM head and keep the mass required to move as low as possible. Self-sensing AFM cantilever with integrated piezoresistive elements are used. All flexures and mounts are milled from aluminum, expect for the AFM head which is 3D printed since it enables a flexible design of arbitrary shapes and allows for easy prototyping.

3.1.2 In-plane with Vibration Compensation

Figure 3.2 shows a 2D concept of the AFM head with vertical actuation mounted to the scanner. For simplicity and low position noise the scanner is operated open loop. Due to creep, hysteresis and other non linearities open loop operation of piezos is far from straight froward [63, 50] and voice coil actuators offer a high range, the scanner is actuated by flexure guided voice coil actuators with low noise current controllers, just like the vertical axis. The much lighter voice coils are mounted to the scanner in order to reduce the moved mass while the heavy magnets are mounted to a fixed frame.

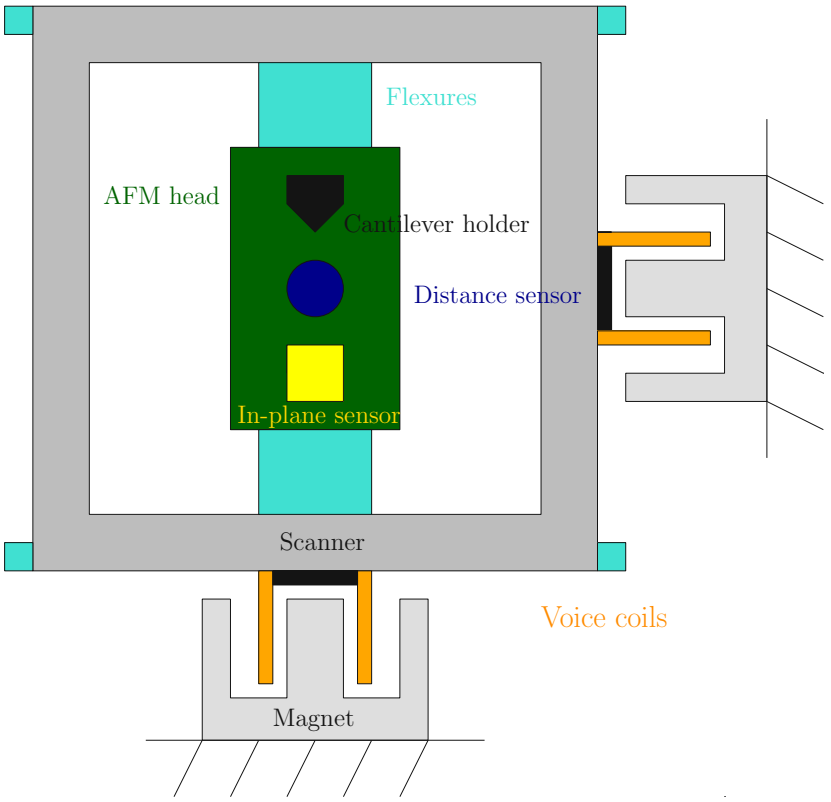

Figure 3.2: Concept for the scanner and the AFM head. The vertical part is mounted in the middle of the scanner. The vertical part carries the AFM head. The AFM head holds the cantilever holder, the additional distance sensor and the in-plane distance sensor, the flexures guiding the in-plane movement are mounted on the edges of the scanner frame. The voice coils are mounted to the scanner and the magnets are mounted to a fixed support frame.

To the knowledge of the Author, there is no literature explicitly discussing the influence of in-plane vibrations on AFM measurements. The in-plane movement of the sample relative to the tip poses a disturbance to the scan trajectory, which results in a height value recorded at a wrong position and therefore leads to a disturbed topography image. In [54] the scan trajectory error induced by thermal vibrations is measured by interfereometers and kept zero by feedback loops. The idea is to also measure and record the in-plane disturbances but with out feedback control, the recorded disturbances will then be added to the planned scan trajectory and consequently the recorded height value is transferred to the position where it was actually measured. The measurement is done favorable with a sensor which needs no markers or specific targets.

In order to verify this idea, experiments with simulated in-plane vibrations on a commercial AFM(Dimension, Bruker, Billerica, USA) are carried out. Figure 3.3 shows an illustration of the experimental setup. The XY-scanner is operated open loop. The external signals were feed in via a signal access module. The XY-piezos are driven by a voltage amplifier (TechProject, Vienna, Austria). The instrument is engaged in contact mode, using the Bruker software. Measurement and signal generation is done with a NI USB card and MATLAB using the data acquisition toolbox. The Z-piezo voltage

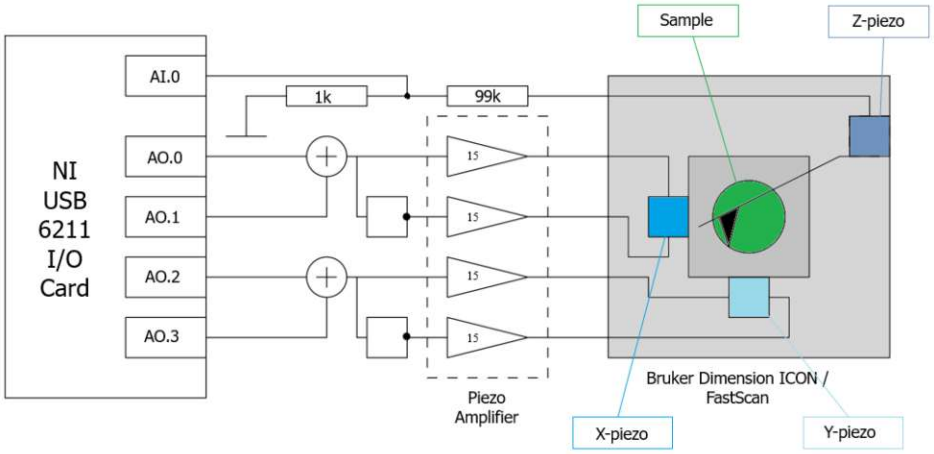

Figure 3.3: Schematic diagram of the in-plane test setup showing from left to right: The I/O card with analog inputs and output, the 1 over 100 probe for high voltage measurement of the Z-piezo voltage, the inverting necessary for operation of the Bruker scanner, the piezo voltage amplifiers and a rough outline of the Bruker AFM

is measured via a 1/100 probe. To scan the sample a trajectory is created,a triangle on the fast axis and a ramp on the slow axis. With this trajectory an area defined by the amplitude and the slope of the ramp is scanned. In addition to the scan trajectory typical vibration profiles are added and applied to the AFM scanner. The distortions are known and simulated in this experiment.

Structural modes, floor vibrations and a combination are applied and the imaging performance is evaluated with topography measurements. Figure 3.4 shows the topography image of a sample with circular test structures measured while the sample is vibrating in-plane. It can be seen that due to vibrations the edges of the circle features are distorted. Excited structural modes are simulated by the sinusoidal signals and floor vibrations are simulated by the band pass filtered white noise inspired by the discussion in Chapter 2.1 The introduced vibrations are sinusoidal with a frequency of 33 Hz on the fast axis and 25 Hz on the slow axis and white noise on both axes. Figure 3.5 shows the result of the post processing compensation on the topography image. The result of the experiment is that as long as the vibrations are measurable the image is reconstructable. This is possible as long as the vertical controller is able follow the sample topography.

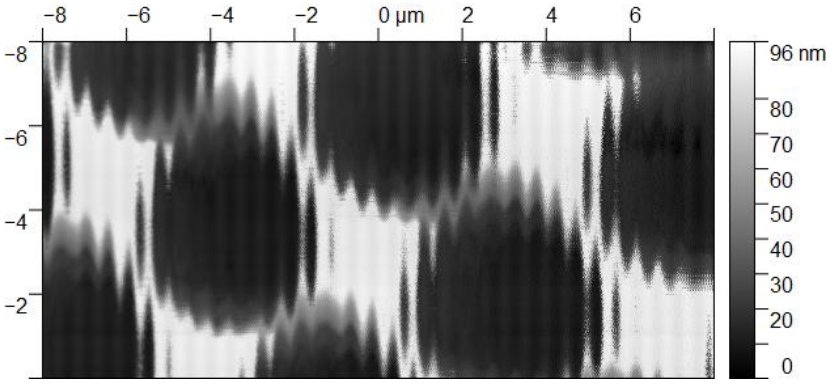

Figure 3.4: Disturbed topography image with in-plane vibrations. The edges of the test structures are distorted.

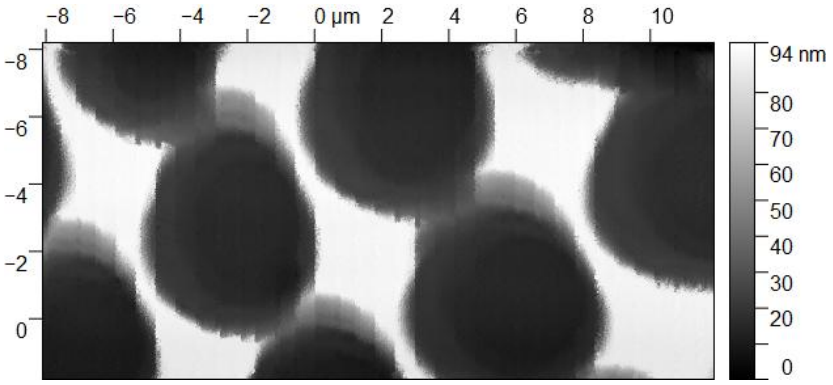

Figure 3.5: Corrected topography image. The scan trajectory error is corrected by the proposed post processing. The edges of the test structures are sharp compared the uncorrected topography image in Figure 3.4.

3.2 Requirements

In order to be easily mountable to mover such as a spindle motor or a industrial robot with vibration compensation platform like presented in [64], the whole AFM assembly should not be larger than 20 x 20 x 15 cm and weigh less than 2 kg. Further this section defines specific requirements like ranges for the actuation.

3.2.1 Scanner

Open loop operation is typically limited to the frequency region below the the first resonance, otherwise the resonance would be excited. Since the scanner is operated open loop, the first resonance frequency of the scanner should be as high as possible in order to achieve a high frequency range. Typically AFM measurements are performed with a fast and slow axis, where the fast axis is perpendicular to the cantilever. Usually a triangle trajectory is driven on the fast axis and a ramp on the slow axis. The frequency of the triangle signal defines the line scan rate. Therefore, a high frequency range is desired in order to achieve high line scan rate. With a given moving mass m the resonance frequency f_r is given by

$$f_r = \sqrt{\frac{k}{m}} \cdot \frac{1}{2\pi}, \tag{3.1}$$

where k is the stiffness of the scanner flexures. Therefore a high stiffness is desired. On the other hand the range is linear declining with higher stiffness for a given actuator force. Therefore there is always a trade off between range and scanning speed.
The scan motion on the fast axis can be described as an average free periodic triangle with the same falling and rising slope in the time domain, in the frequency domain it can described as superposition of n sinusoidal signals with its harmonic frequencies f_n given by

$$f_n = f_0 \cdot (2n - 1) \tag{3.2}$$

and the amplitudes a_n of the harmonics are given by

$$a_n = \frac{1}{(2n-1)^2}. \tag{3.3}$$

The scanner should at least be capable of scanning at a line scan rate of 1 Hz. Assuming that after the first 5 harmonics the amplitudes are already low enough that the higher harmonics do not lead to a significant excitation of the scanner. To reach 1 Hz line scan rate the first resonance of the scanner has to be higher than 9 Hz. Typically AFMs have a scan range of approximately 100 μm. The here designed setup should be capable of scanning at least a similar area. Therefore, the required range is increased to 150 μm to have a margin of error.

Range X	150	μm
Range Y	150	μm
Open loop BW	> 9	Hz

3.2.2 Vertical Actuation

As discussed in Chapter 2.1 typical frequencies for vibrations start at 0.5 Hz and reach several 10 Hz. Therefore, a good vibration rejection at low frequencies is required. The sensitivity to a disturbance on the output of a feedback controlled system is given by the sensitivity function. The sensitivity function of a feedback controlled linear system is declining with 20 dB per decade with declining frequencies starting from -3 dB frequency of the closed loop system therefore the controller bandwidth should be as high as possible. As magnitude 1 Hz is selected based on the 880 Hz reached in [51] is used. The vertical range is necessary to compensate for imperfect sample placement and vibrations. Typical peak amplitudes are up to 10 μm as discussed in Chapter 2.1. and a sample tilt of 15 μm should be compensateable, therefore a range of 25 μm is required.

Range X	25	μm
Closed loop BW	1000	Hz

3.3 Sensor and Actuator Selection

3.3.1 Cantilever Selection

As discussed in Chapter 2.3 cantilevers with piezoresistive elements enable compact and light weight deflection measurement because no optical path and photo detector is required for deflection measurement. Commercially available self-sensing AFM cantilevers (PRSA-L300-F80-Si-PCB, SCLSensortech, Vienna, Austria) with two integrated piezoresistive elements at their base which are interconnected as a half bridge circuit on the chip are used. They are used because they are light, less than 2 g and compact with a connector size of just 6 x 6 mm.

3.3.2 Sensor Selection

The compensation of tip-surface vibrations as proposed in Section 3.1 requires a high precision measurement of the distance between the AFM cantilever and the sample. The performance of the distance sensors directly limits the achievable resolution of the topography image in out-of-plane and in-plane direction. The sensors should therefore have a high position resolution and sufficient range to enable a measurement over the measurement range specified in the previous section. In addition to the measurement range required by the scan motion, the out-of-plane sensor requires sufficient range to enable a reliable sample approach process without risk of damaging the cantilever or the sample. Additionally, a high bandwidth is required to be able to track the fast tip-surface distance variations due to high frequency vibrations and the AFM scan motion. Since the sensors are mounted on the moving AFM-head as shown in Figure 3.1, they should have a small size and low weight. Finally, a contact less distance measurement without dedicated target is preferred to enable in-line measurements on arbitrary samples.

For the out-of-plane measurement, a number of different measurement principles come into consideration. The most widely used distance sensors are based on an optical, inductive or capacitive measurement principle [65]. Optical distance sensors have high bandwidth and offer sub-nm resolution over a large range. However, they require reflective targets and have a small measument spot size and are therefore influenced by topography on current position. Capacitive and inductive sensors enable distance measurements to targets of arbitrary material and reflectivity. In this work, a capacitive distance sensor is used as out-of-plane distance sensor due to its superior position resolution with respect to inductive distance sensors. The used sensor also works on non conductive targets. The sensor measures the average distance to the target in a circular spot with a diameter of approximately 3 mm. This average distance measurement is crucial for the presented out-of-plane measurement concept to work. If the spot size is not much larger than the expected features of the topography the sensor would not only measure the distance between sample and AFM head but also the sample height at the current position. The out-of-plane sensor should have a large range to enable an automated tip sample approach mechanism. As additional out-of-plane distance sensor a captive distance sensor (CSH-05 Micro-Epsilon Messtechnik, Ortenburg, Germany) with 0.5 mm range and a resolution of 10 nm rms is used. It is selected because it is compact and light. Furthermore is has a large measurement spot spot size. A second captive distance sensor (6810, MicroSense, Hamm, Germany) is used as evaluation distance sensor in Chapter 4.

For the in-plane measurement a sensor with out the necessity of a marker is favored for in-line measurements [57]. Therefore the PMW3360DM-T2QU form (PixArt Imaging Inc., Hsinchu, Taiwan) is selected as in-plane displacement sensor with a custom build read out box, described in detail in [58]. This sensor is based on measuring the movement of optical laser speckles [55]. The sensor has to be mounted on the AFM head as the resolution of the sensor depends on the distance to sample and the AFM head is in nearly constant distance to the sample due to feedback control. The sensor is designed as displacement sensor used in optical computer mice. The read out box provides two channels representing the displacement on two axes. The sensor is compact with dimensions of 27 x 22 mm and light. The resolution of this sensor is 2.12 μm this is just suitable for long range AFM imaging. It is tried to proof the concept of marker and target less in-plane measuring during long range AFM imaging in this work.

3.3.3 Actuator Selection

For the actuation in the nanometer range piezo actuators and Lorentz actuators come into consideration. As stated in Chapter 3.1 the scanner should be operated open loop. Due to creep, hysteresis and other non linearities open loop operation of piezos is difficult [63, 50]. For the required range of the vertical axis piezos are not offering a higher bandwidth as flexure guided Lorentz actuators. As suggested by literature discussed in Chapter 2.4 flexure guided Lorentz actuators are capable of enabling long range AFM imaging with high resolution. The actuators are typically driven by current controllers because voltage changes due to the back electromotive force of the moving coil are not affecting the actuation force. The position accuracy of a flexure guided Lorentz actuator is primarily depending on current controller output noise with given

stiffness of the flexure. In [51] a vertical resolution of 2.9 nm is achieved with a flexure guided voice coil actuator. As the selected additional out-of-plane distance sensor has a resolution of 10 nm the position accuracy of the vertical axis should be better than that. The tip of the used cantilevers has a diameter of approximately 30 nm. Therefore, the resolution of the in-plane axes should be in the same range or better otherwise the topography image performance of the designed setup is limited by the scanner. Lorentz actuators in the form of Voice coil actuators (CVC26-SF-7, PBA Systems, Singapore, Singapore) with 3 N continues force at 100 degrees Celsius and 17.11 N peak force are used for all axis. They are used because they are compact and offer a good weight to force ratio. The actuators have stroke of 7 mm which is more than necessary in this work but they are the shortest commercially available ones with required force. Furthermore, their documentation stated a low dependency between force and displacement which is crucial for open loop operation. The dependency between force and displacement can be neglected in the 100 μm range. For the actuation of the scanner a so called push-pull principle is used. This means for each scanning direction two pairs of voice coil actuators, which are in opposite phase with each other, i.e. one is pulling while the other one is pushing, as suggested in [49]. This can improve the range and leads to a mechanically balanced system reducing recoil.

3.4 Experimental Setup Design

As all sensors and actuators are selected the flexure based AFM is designed around them and the given requirements. Figure 3.6 shows an assembly of the AFM setup. The 3D printed AFM head is pictured in dark gray. On the AFM head is the capacitive distance sensor right in the middle in green, the hole for the lens of the in-plane mouse sensor right of the vertical distance sensor and the place for the cantilever holder left of the distance sensor. The coils of the actuators are in orange. The two pairs of voice coil actuators for both in-plane axes and a single one in the middle for the vertical axis. The scanner is guided and hold by flexures, see Figure 3.2 also. The vertical support frame holds and guides the vertical moving platform with flexures and is mounted to the scanner, see Figure 3.1 also.
All signal processing and recording is performed with a rapid prototyping system (dSPACE, Paderborn, Germany) with 16bit ADCs and DACs.

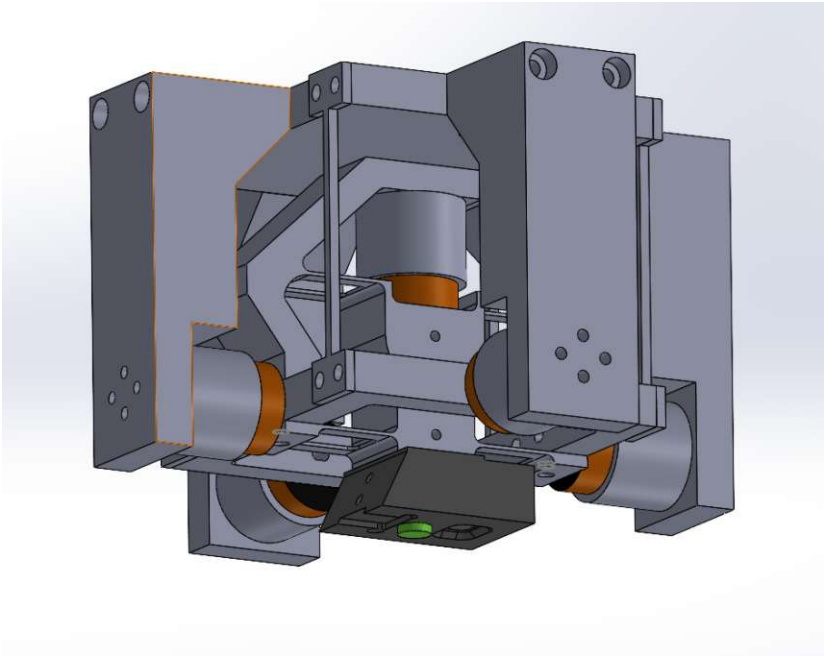

Figure 3.6: Assembly of the AFM setup. The AFM head in dark gray with the capacitive distance sensor in green, the hole for the mouse sensor right of the distance sensor and the place for the cantilever holder right of the distance sensor. Coils are in orange. The two pairs of voice coil actuators for both in-plane axes and a single one in the middle for the vertical axis. The scanner is guided by flexures. The vertical support frame guides the vertical moving platform with flexures and is mounted to the scanner.

3.5 Flexure Design and Modal Analysis

All flexures and support frames are CNC-milled from aluminium 6082 alloy with an of E-modulus of $E = 70 * 10^9\ N/m^2$, (70 GPa) [66].

3.5.1 Vertical Actuation

The desired stiffness k_d for the flexures is given by

$$k_d = \frac{F_{vca}}{r_v} = \frac{3N}{50\mu m} = 60000N/m, \tag{3.4}$$

where F_{vca} is the continuous force of the voice coil actuator and r_v is the required range out-of-plane respectively vertical. The desired range is the doubled necessary range to account for possible manufacturing tolerances and give margin of error. The dimensions of the beam shaped flexures are limited by the smallest millable structures given by the supplier with 0.5 mm and design limitations caused by the selected sensors and actuators, resulting in a length l of 20 mm and a thickness b of 4 mm. The moving part is guided by 8 flexures. With 4 flexures as in Figure 3.1 and the milling limitations the flexures would have to be longer than 20 mm and the design would not be as compact

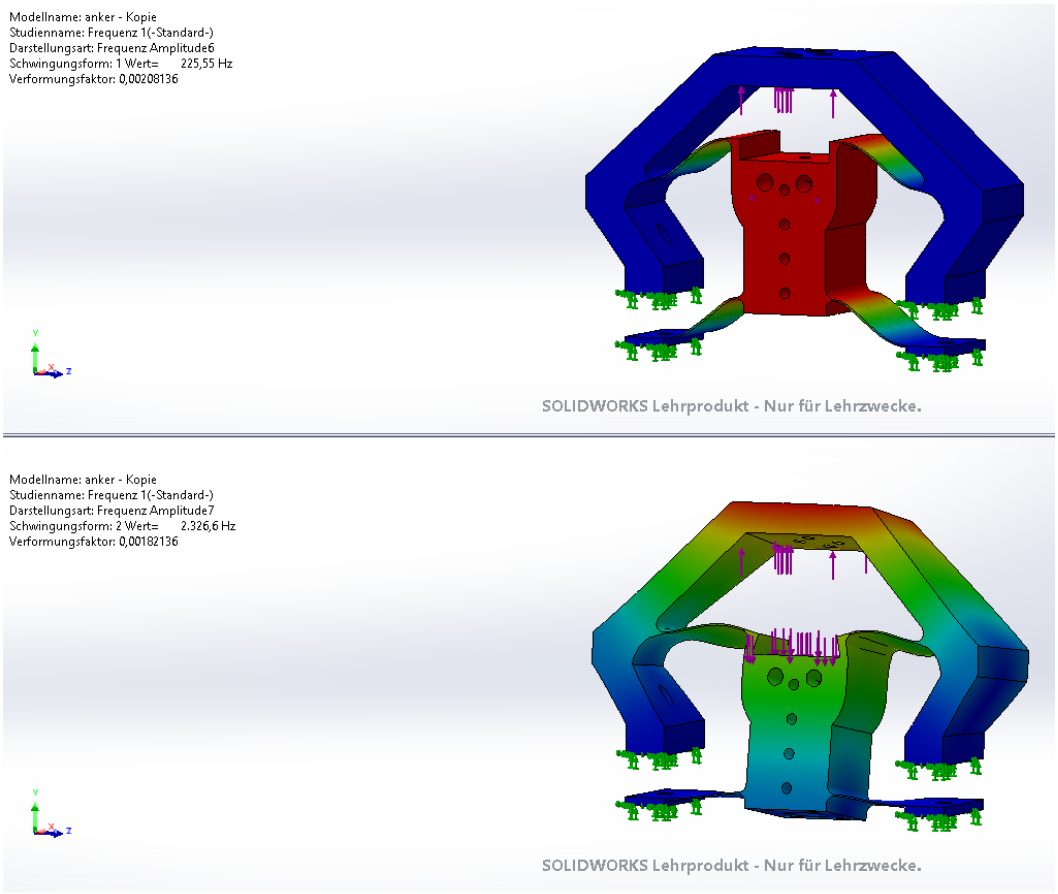

Figure 3.7: Results of the SolidWorks modal analysis. The upper part shows the suspension mode as first mode shape with an eigenfrequency of 225 Hz. The lower part shows the tilt mode as second mode shape with an eigenfrequency of 2326 Hz.

as desired anymore. The required flexure height is calculated by

$$h = (\frac{k_d \cdot l^3}{n_{flex} \cdot E \cdot b})^{\frac{1}{3}} = 0.6\,mm \tag{3.5}$$

where n_{flex} is the number of flexures in the direction of interest, E is the e-modulus of the used aluminum and b, l and k_d are the thickness, the length and the desired stiffness of the flexures, respectively. The formula is an approximation for small displacements rearranged from [67, 68]. Since this is only an approximation a finite element simulation using SolidWorks is also done to verify the calculations. The static simulation confirms the calculation, with 3 N force a displacement of 48 mm is reached. As the vertical axis is actuated by a single actuator, there is no way to compensate for tilt and rotational modes. A modal analysis is conducted in order to verify that higher mode shapes are accruing above the desired controller bandwidth of 1 kHz, since we are not expecting vibrations above 200 Hz as discussed in Chapter 2.1 the higher modes are not excited if their eigenfrequencies are high enough.

Figure 3.7 shows the first two mode shapes. The first six structural modes of the vertical actuation are simulated with SolidWorks Modal-analysis. The first mode is the suspension mode at 225 Hz which is observable by the vertical sensors(cantilever, additional vertical distance sensor) and can be damped by feedback control. The second mode shape shows the tilt mode which is not observable with the chosen sensor placement, neither would it be controllable with the single actuator concept but since its eigenfrequency is 2326 Hz it will not be excited.

3.5.2 Scanner

The scanner is guided by a flexure on each edge of the square moving scanner frame so four beam flexures are used in total. The scanner can be seen in Figure 3.2 and Figure 3.6. The calculations are assuming that only one actuator is used, the push-pull principle is used later to extend the range of the scanner. The length of the beam shaped flexure is a design decision, set at 60 mm in order to have enough space for vertical actuation and the additional out-of-plane sensor. The footprint of the beam must be a square in order to achieve the same stiffness for both axes, this means that both axis can be used interchangeable as fast axis for scanning. The desired stiffness k_d for the flexures is given by

$$k_d = \frac{F_{vca}}{r_i} = \frac{3N}{150\mu m} = 20000N/m, \tag{3.6}$$

where F_{vca} is the continuous force of the voice coil actuator and r_i is the required range in-plane. The flexure side length a necessary to achieve the desired stiffness is calculated by

$$a = (\frac{k_d \cdot l^3}{n_{flex} \cdot E})^{\frac{1}{4}} = 2mm, \tag{3.7}$$

where k_d is the desired stiffness, n_{flex} is the number of flexures in the direction of interest, E is the e-modulus of the used aluminum and the flexure length l. The formula is an approximation for small displacements rearranged from [67, 68]. The same simulations as for the vertical actuation are carried out. The static simulation confirms the calculation, with 3N Force a displacement of 153 μm is reached. The eigenfrequencies of the suspension modes of the in-plane axes are 60 Hz and 61 Hz, the fist tilt mode occurs at 93 Hz. The simulations show that the designed scanner is capable of 1 Hz line scan rate.

The AFM is designed in this chapter, based on selected sensors and defined requirements. The designed parts are milled and the proposed setup is assembled and evaluated in the next chapter.

CHAPTER 4

Implementation, Evaluation and Controller Design

In the previous chapter the AFM setup was designed and simulated. The setup is now assembled and tested. Practical experiments are carried out to evaluate and verify the performance of the design. The experiments are separated in scanner and vertical actuation tests. The results of the performance evaluation are compared to the simulations in the previous chapter. A topography measurement on a test grating is performed in order to verify the functionality of the AFM without vibrations. In order to achieve a good disturbance rejection a model based high bandwidth controller is designed. The chapter is structured into experimental setup presentation, scanner evaluation, vertical actuation evaluation, in-plane sensor experiments, AFM topography imaging evaluation and high bandwidth controller design. The voltage measurements and signal generation in this chapter are performed with an Analog Discovery 2 System analyzer (Digilent, Pullman, Washington, USA) unless stated otherwise.

4.1 Experimental Setup

Figure 4.1 shows an overview of the built setup. On the bottom left the current controllers are visible. For each actuator a current controller capable of 3 A bipolar is used. The current controllers are supplied with 15 V for the control electronics and 30 V bipolar for the power part. The AFM assembly is mounted on 50 x 50 mm aluminum profiles arranged in an U-shaped structure. Below the AFM assembly the manual stages for sample poisoning are shown. A single micrometer stage (Thorlabs Inc. Newton, New Jersey, USA) for each of all 3 axis is used, each are offering μm positioning accuracy and a range of 25 mm. A piezo stage (nPoint, Middleton, WI 53562, USA) with 100 μm range on two axis is used to apply vibrations to the sample. The piezo stage is mounted to the manual stages and moves the sample holder. This details are also well visible in Figure 4.2 (a). On the right side is the blue white demodulation box for the additional out-of-plane distance sensor. In the upper right part of Figure 4.2 (b) is the custom

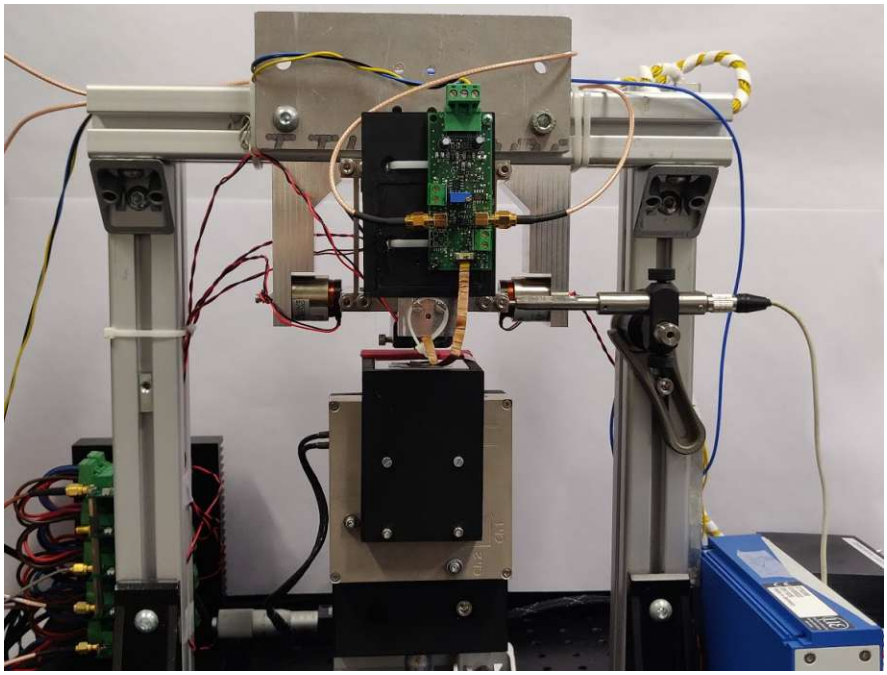

Figure 4.1: Image of the assembled setup showing from left to right: 5x current controllers with cooling for the voice coil actuators, aluminum profile mount, AFM assembly, sample positioning stages with the stainless steel sample holder on top, MicroEpsilon capacitance sensor demodulation box, verification capacitve distance sensor and the in-plane mouse sensor readout box.

built deflection measurement printed circuit board for the piezoresisitve cantilever It consists of voltage regulators for the supply voltages, an instrumentation amplifier for the half bridge output voltage and an offset correction. The output voltage of the instrumentation amplifier is applied to a voltage follower and connected to the dSPACE ADC. The AFM-head is in the bottom middle of Figure 4.2 (b). The gold chip holds the cantilever and is connected to the deflection measurement printed circuit board via a ribbon cable. The in-plane distance sensor and the additional out-of-plane sensor are integrated in the black 3D printed AFM head. Can be seen with more details in Figure 4.3. The assembled AFM including the scanner, the AFM head, the deflection measurement electronics and the support frame has the following dimensions 16.5 cm wide, 16.5 cm deep and 12 cm high and weighs 1534 g including cables.

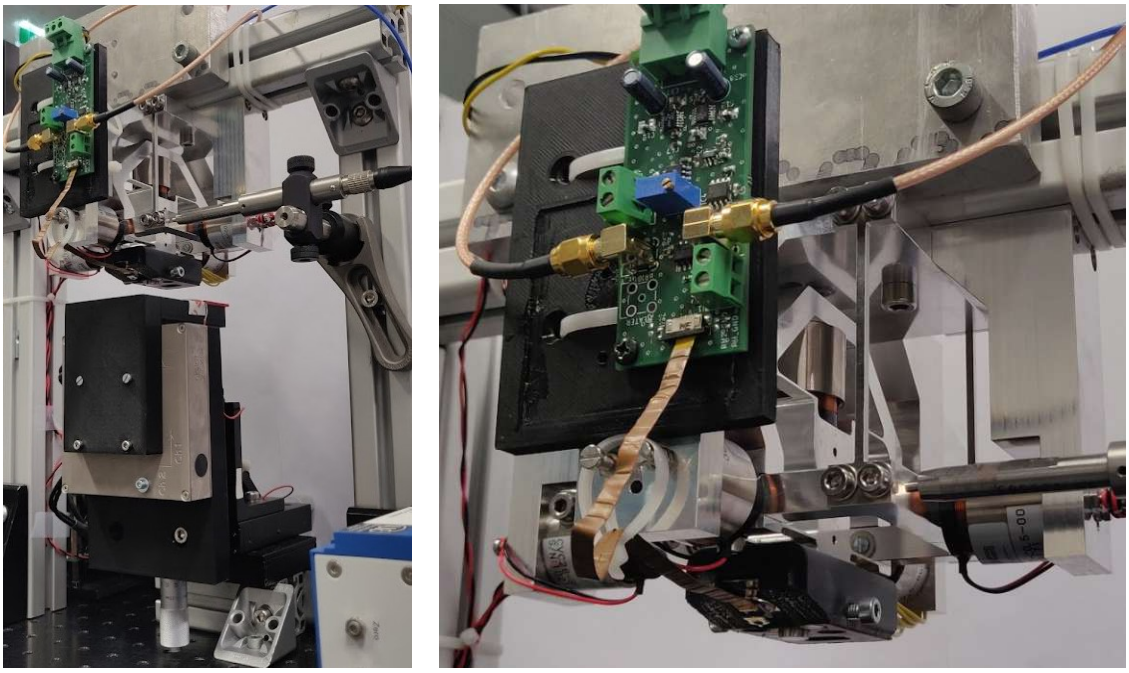

(a) (b)

Figure 4.2: Details of the assembled setup. Figure (a) shows the manual micrometer stages to position the sample precisely under the AFM assembly and the nPoint piezo stage for the sample vibrations on the bottom. Figure(b) shows the deflection measurement printed circuit board, the AFM head with more details in Figure 4.3, and the flexure guidance

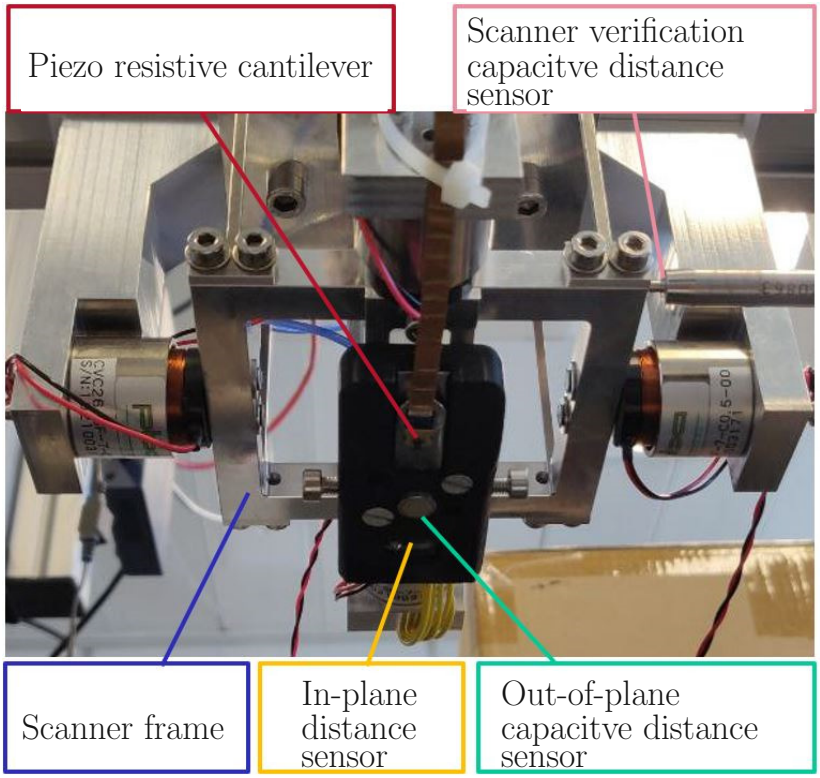

Figure 4.3: Detailed image of the AFM-head and sensor placement.

4.2 Scanner Evaluation

To evaluate the scanner performance the evaluation distance sensor is used. It has a range of 100 μm, a sensitivity of 5 μmV and a position noise of 5 nm_{rms} is used. In this section the linearity, the frequency response and the positioning accuracy of the scanner is evaluated.

4.2.1 Linearity

In this experiment, the linearity of the scanner is analyzed. A triangular reference voltage is applied to the current controller. Figure 4.4 shows the measured displacement over the reference voltage. The data of a full period of the triangle signal is plotted. As expected the graph shows a highly linear relation between reference voltage input and the resulting scanner displacement. No hysteresis is observable.
Since the range of the MicroSense sensor is limited to 100 μm, and it is not perfectly mounted at half range the linearity experiment is limited to a triangle trajectory with an amplitude of 35 μm. This is not a problem since later in the thesis long range experiments on a test grating are presented. The scanner is highly linear and therefore suitable for open loop operation.

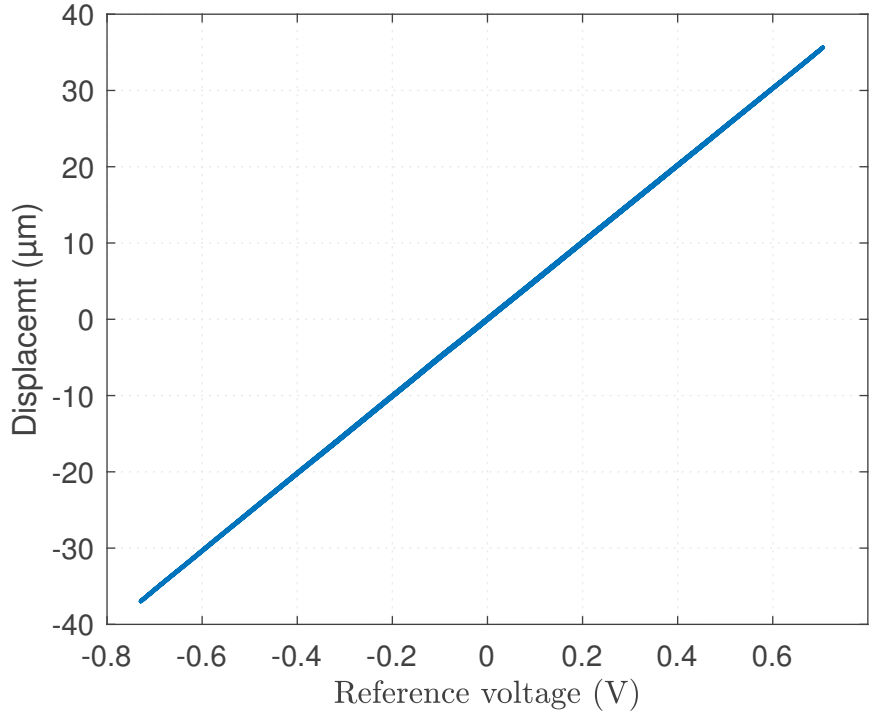

Figure 4.4: Displacement plotted over reference voltage applied to the current controller. The plot shows high linearity and no hysteresis.

4.2.2 Dynamics and Positioning Accuracy

Frequency Response

In this experiment the resonance frequencies of the scanner are determined. Figure 4.5 shows the frequency response of the reference voltage applied to one scanner axis to the measured displacement. The first resonance has a frequency of 42.3 Hz and is as intended significantly higher than the 5th harmonics of for 1 Hz line scan rate. Anti resonance and resonance at 50.9 Hz and 65 Hz, respectively, are probably due the to tilt mode of the scanner. This can be explained by the sensor position. The distance sensor is positioned at the edge of the scanner, as shown in Figure 4.6 and Figure 4.3. This means it measures displacement and tilt. It can not be distinguished between tilt and suspension mode. It is not possible to mount the sensor exactly in the middle of the scanner to measure just the suspension mode because the actuators are in the way. The second resonance is probably the tilt mode this is suggested by the simulation and an additional experiment with the sensor placed closer to the center of the scanner, where the second resonance peak declined from 16db to 12.5 dB while the first one stayed at approximately 15 dB(data not shown). With 42,3 Hz the first resonance is lower than the simulated 60 Hz this might be caused by the ignored weight of the screws and other small parts.
The fist resonance is high enough for open loop operation of the scanner at 1 Hz line scan rate which is discussed in more detail in the following section.

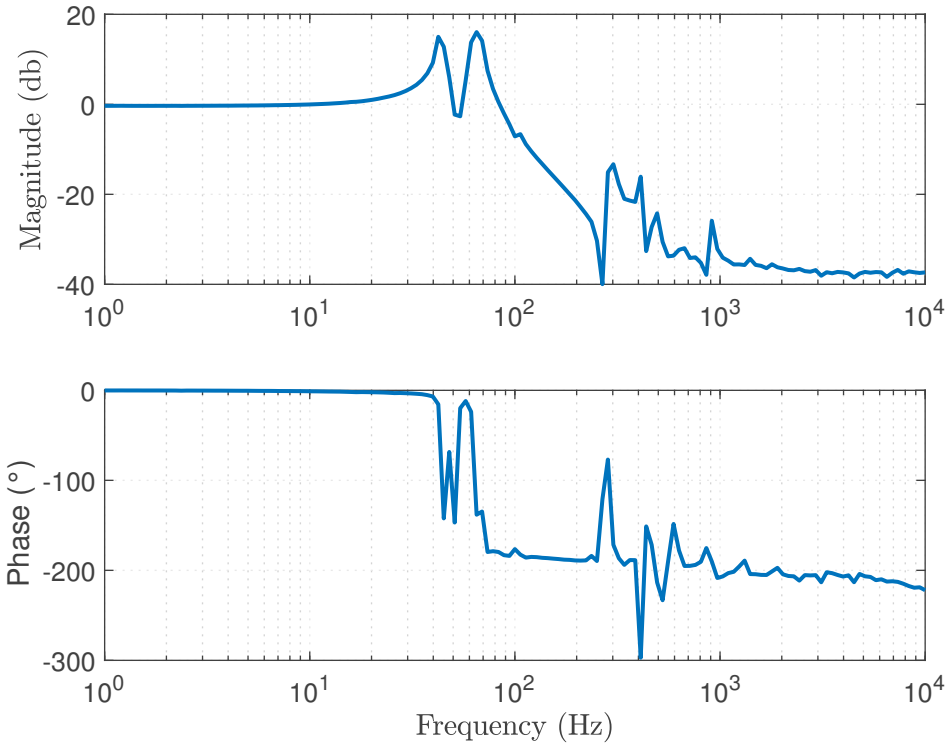

Figure 4.5: Frequency response of the scanner axis measured from the reference voltage applied to the current controller to output of the verification distance sensor. The first resonance frequency is at 42.3 Hz.

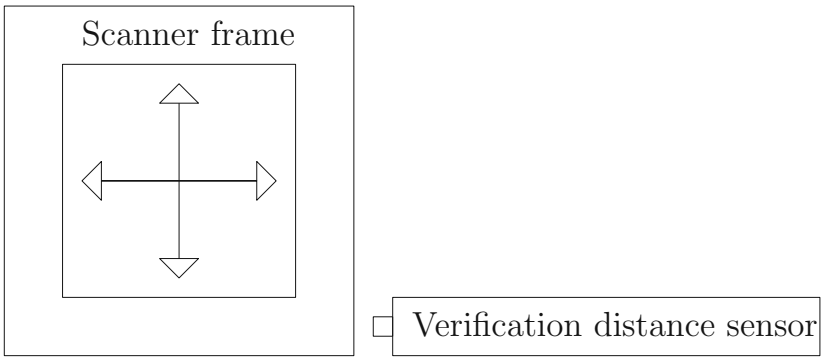

Figure 4.6: Sketch showing the scanner verification distance sensor placement.

Scan Trajectory Experiment

The scan trajectory during AFM topography imaging is typically a triangle on the fast axis. To verify that the scanner dynamics are not excited a periodic triangular reference signal is applied. Figure 4.7 shows the applied triangular reference signal and the measured scanner position. The scanner is able to follow the triangle trajectory. The rising slopes are called traces and the falling slopes are called retraces. Traces and retraces are parallel. The last 1 μm before and after the direction change will be cropped from the AFM images, which allows higher scan rates because the absolute position error of the scanner is here at its maximum. The deviation of the measured position from the reference triangle is shown in Figure 4.8. The sensitivity to the higher harmonics of the scanner is higher than expected. The higher harmonics of the 1 Hz triangle are exciting these modes, well visible in Figure 4.8 looking at the blue plot. In order to prevent that from happening, a pre filter 4th order with a cut-off frequency of 15 Hz for the scan trajectory is used. This filter is implemented via dSPACE. Figure 4.8 shows the position error with a pre filtered trajectory in orange and in blue without pre filtering.
With the 15 Hz pre filter the higher harmonics of the scanner are not significantly excited. The scanner can be operated at 1 Hz line scan rate, see Figure 4.7 which is measured with the pre filter already implemented.

Positioning Accuracy

In order to determine the resolution of the scanner it is positioned at constant position ($x = 5\,\mu m, y = 10\,\mu m$) with the according input signals. Since only the alternating part of the measured signal is of relevance for this experiment the average free rms value of the scanner position is measured. The resolution is $16nm_{rms}$ at a constant position on one axis. The resolution is probably limited by the current controller noise. However the position resolution is of similar size than the typical tip radius of AFM cantilevers. Therefore the position noise of the scanner should not limit the AFM imaging performance.

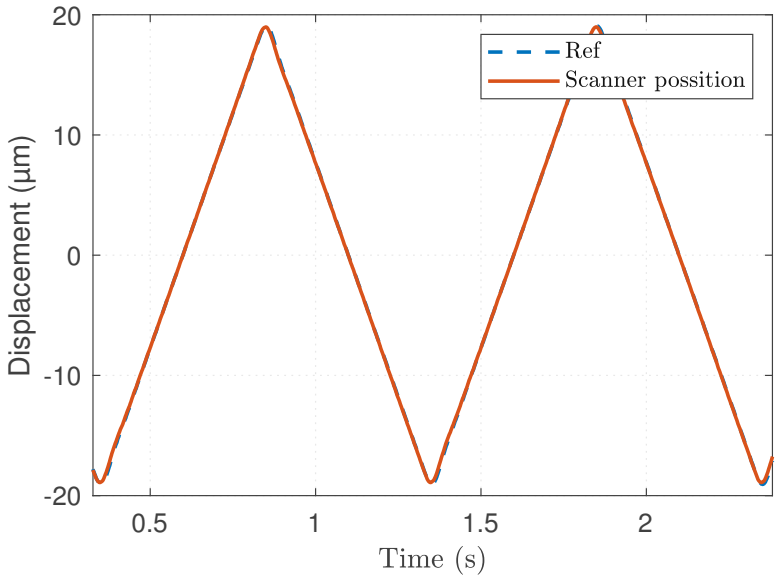

Figure 4.7: A reference triangle trajectory is plotted in blue. The orange plot shows the measured scanner position. It is clearly visible that the scanner can follow the reference signal.

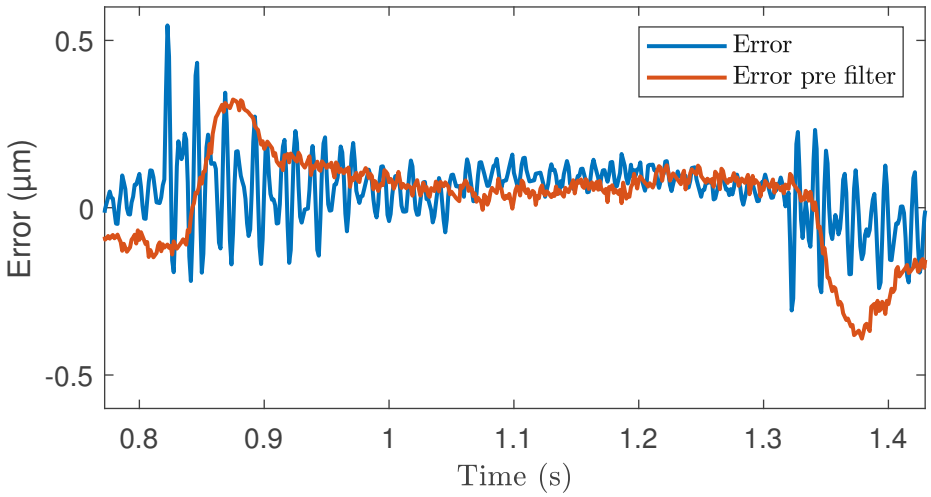

Figure 4.8: Position error of the scanner, with pre filter in orange and without in blue. With the 15 Hz pre filter the higher harmonics of the scanner are not significantly excited. With out a filter the direction change excites the higher harmonics.

4.3 Vertical Actuation

In this section the frequency response of the vertical actuation is analyzed and compared to the simulation and calculation presented in Chapter 3.5.1. Figure 4.9 shows the frequency response of the vertical actuation. The frequency response of the vertical axis is measured using the capacitive vertical distance sensor. The first resonance of the vertical axis is at 236 Hz. The simulation presented in Chapter 3. resulted in the the transfer function

$$P(s) = \frac{scale}{(ms^2 + cs + k)} = \frac{35718}{s^2 0.0290 + 2.8s + 59530} \tag{4.1}$$

in Laplace domain where m is the moved mass of the AFM head and the moving platform, c the damping, k the stiffness of the axis and the *scale* factor models the sensor sensitivity. The frequency response of the simulated transfer function (4.1) is plotted in orange. The measured frequency response closely matches close the simulation, except for a deviation of the phase above 300 Hz. This deviation can be explained by a phase lag of the used distance sensor. Although according to the data sheet the sensor has a bandwidth of 8 kHz, a phase of approximately 20 degrees due to the sensor is already visible in Figure at 1 kHz. The measured first resonance frequency of the axis is 236 Hz which is a deviation of 11 Hz only from the simulated 225 Hz.

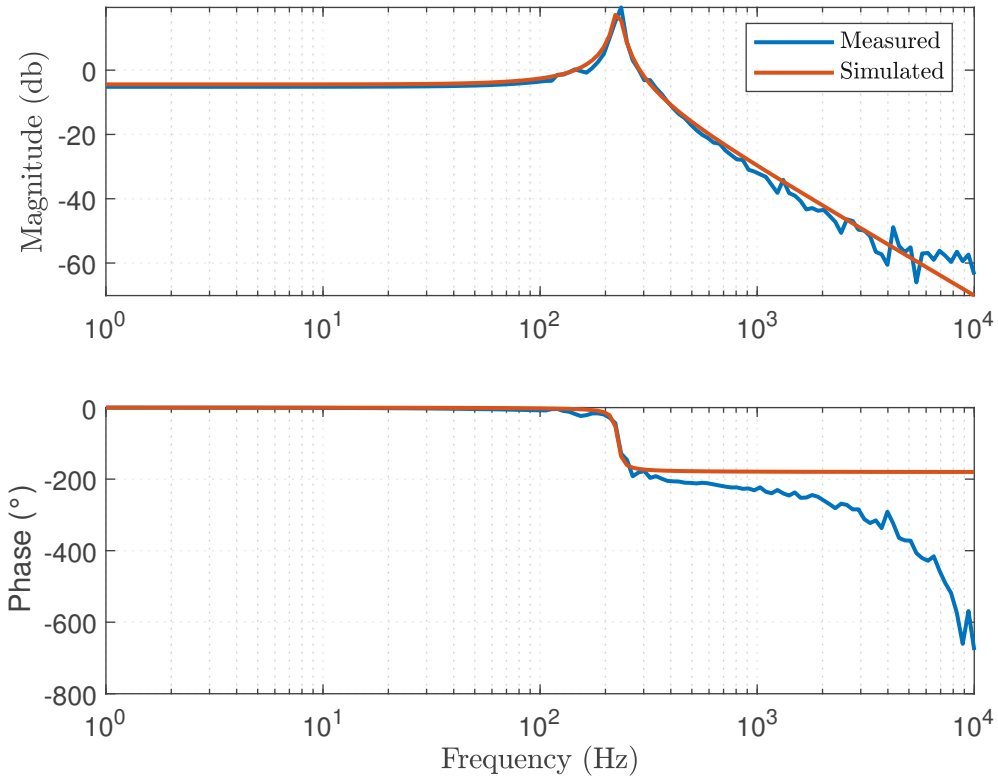

Figure 4.9: Frequency response of the vertical axis measured from the input voltage of the current controller to the vertical displacement measured by the capacitive vertical out-of-plane distance sensor. The fist resonance of the vertical axis is at 236 Hz. The simulation fits the measured data well, except for the phase above 300 Hz, due to sensor phase lag.

4.4 In-plane Sensor Experiments

The in-plane distance sensor should measure the position of the AFM head relative to the sample. A mouse sensor with a custom built read out box is used which provides a position signal on two axes. Experiments regarding the in-plane distance mouse sensor are presented in this section. The sensor is called just mouse sensor in this section. The scanner is moved in typical scanning motion, a triangle on the fast axis and a slope on the slow axis. The displacement during scanning is measured with the mouse sensor as evaluation experiment. Figure 4.10 shows measured displacement on the fast axis. The applied triangle reference has an amplitude of 40 μm. Although the triangular signal can be seen in the measured data the error is large. The mouse sensor is not capable of following the reference triangle. Drift is occurring and blind spots are visible, further examples are shown in Figure 4.11. The mouse sensor shows drift in the 100 μm range well visible in Figure 4.11 (a). Blind spots in the 10 μm range are occurring an example is given in Figure 4.11 (b).

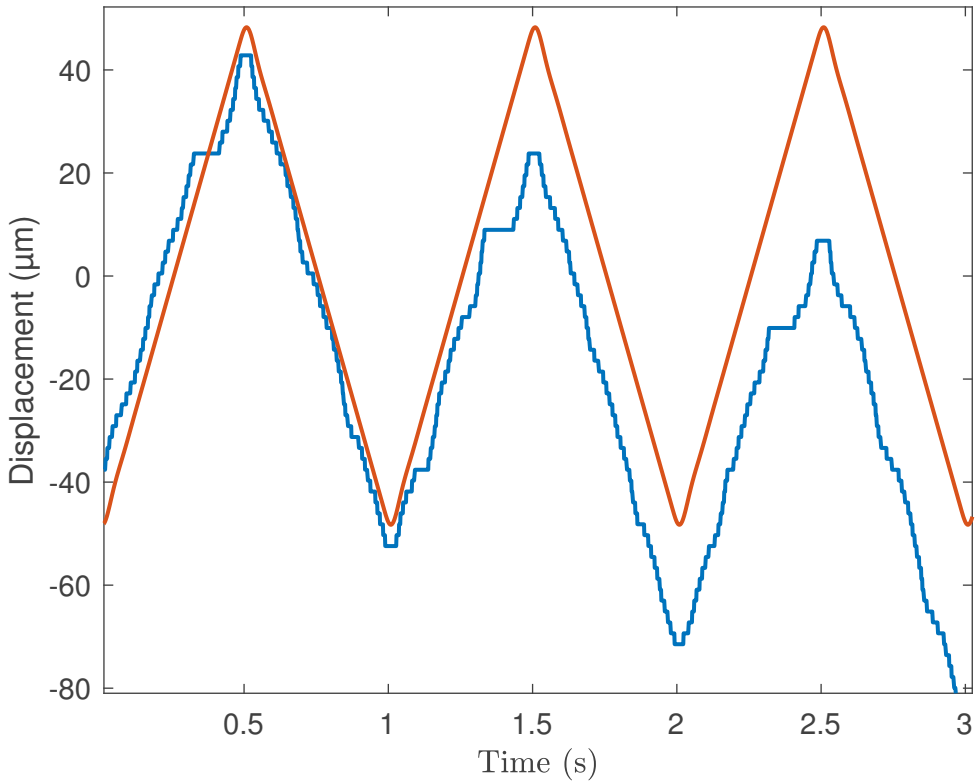

Figure 4.10: In-plane mouse sensor test, the displacement of the fast axis is measured using the mouse sensor. Measured data is plotted in blue. The reference triangle is plotted in orange. Drift and blind spots can be seen.

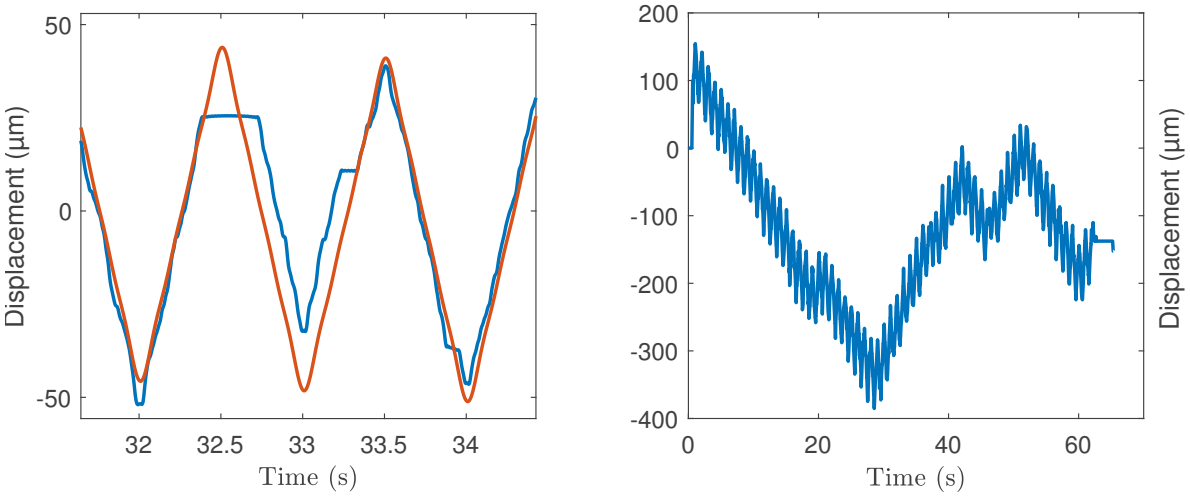

(a) (b)

Figure 4.11: In (a) an example of a blind spot is shown, reference trajectory in orange and the measured signal in blue. The blind spot leads to an error of approximately 15]μm. (b) shows a sensor drift example, no deterministic drift pattern is observable.

The Sensor is not usable for any real-time operations like feedback control with this strong drift characteristics. Furthermore there is not really a deterministic drift pattern observable, this means easy line fitting methods for drift subtraction are not working. The best working post processing method for drift rejection is found to be forward backward zero phase high pass filtering [69], further a low pass is applied to reduce quantitation edges. This was done with a high pass with infinite impulse response and a filter order of 8 and a passband frequency 0,2 Hz, the result for a post processed triangle trajectory is shown in Figure 4.12.

As possible post processing procedure to obtain the in-plane vibrations it to apply the same filters to the known trajectory and the measured signal so scaling due the filters effects both in the same way and subtract them in order to get the vibrations.

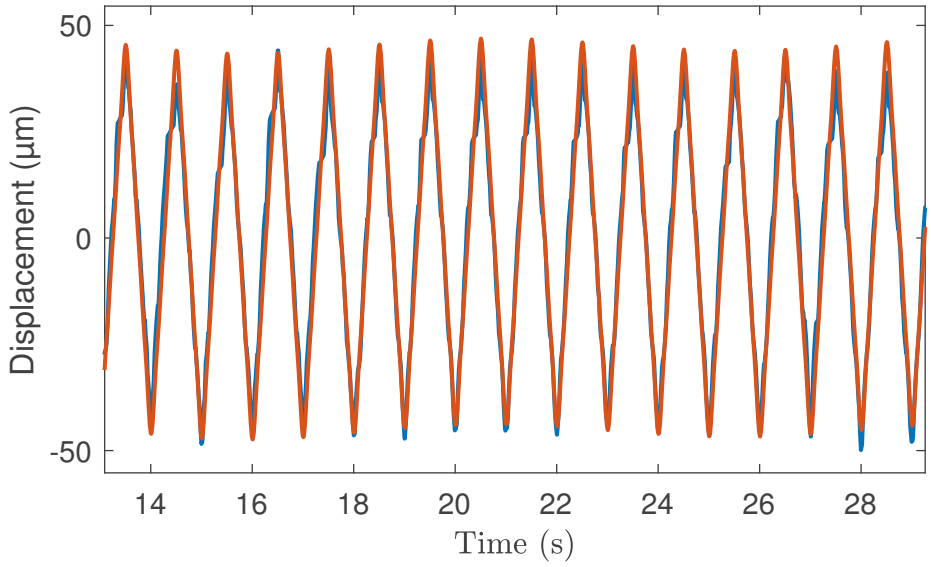

Figure 4.12: Filtered signals, triangle trajectory in orange, measured signal in blue. The triangle can be followed with a limited error.

Furthermore there is an effect similar to a velocity threshold. The slow movement of the slow axis is not measurable while scanning. Several different target surfaces like 3D printed PETG, stainless steel, masking tape, and cellular rubber are tried, pink cellular rubber works best. The software on the sensor is proprietary, so no further insights on the intern signal processing is possible. As its main purpose is the use as mouse sensor, it might be optimized for different ranges and speeds as the human hand position accuracy is in the millimeter range [70].
Since the slow axis is not measurable with this sensor and the large blind spots the sensor is not used for AFM-imaging later on. The velocity threshold was not expected neither were the blind spots.

4.5 AFM Imaging

The setups capability of AFM topography imaging is evaluated in this section. A test grating with 100]nm high squared pits and a pitch of 10 μm is scanned. The sample is placed on the sample holder and the tip is brought into contact with the sample with manual stages. The sample is not vibrating during this experiment. An integral controller is used to maintain a constant tip sample force. Figure 4.13 shows the measured topography image with a plane fit to eliminate the sample tilt. The image consists of 480 scan lines and has a resolution of 492 x 480 pixels. One scan obtains two images the trace and the retrace. The scanner moves forward and backwards in fast-scan direction, while moving slowly toward slow-scan direction. The trace image is formed from left-to-right motions and the retrace image from right-to-left motions [71]. The line scan rate is 1 Hz. The fast axis is the horizontal one in all following AFM images. Figure 4.13(a) shows obtained the topography image. Just the retrace is plotted. As

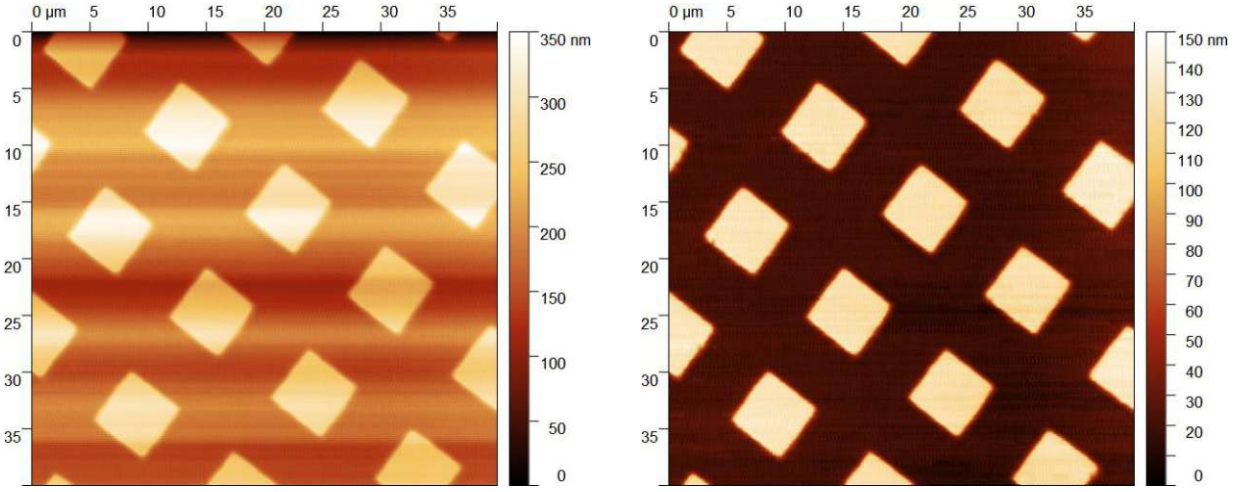

(a) (b)

Figure 4.13: Figure (a) shows a constant force AFM topography image with a plane-fit to compensate the sample tilt. Figure (b) shows the same AFM topography image with a plane-fit and a line-fit against the slow drift.

expected the squared features have a size of 5 x 5 μm and have a height of 100 nm. A vertical resolution of 3 nm rms is achieved. This is the average of four different flat horizontal lines along the fast axis. All edges of the features are sharp. In Figure 4.13 (a) a drift on the slow axis is visible. This drift shows time constants of around 30s and is due to air circulations which change the temperature of the piezorestive elements which show a strong temperature depending resistance. One solution for the drift would be a housing to prevent the circulations which is used for the measurements in [44, 45] where the same cantilevers and similar electronics are used. Figure 4.13 (b) shows the same topography image with a line fit applied. The signal recording is done via dSPACE using the mlib library. The post processing is done using Gwyddion. This low bandwidth feedback controller is not capable of faster topography imaging and would not provide good performance on a vibrating sample. In the next section a high bandwidth controller is designed. The AFM works as intended except for the temperature drift. Once the high bandwidth controller is designed experiments with a vibrating sample can follow.

4.6 Controller Design

In this section the high bandwidth controller for the vertical axis an the out-of-plane disturbance rejection is designed. The controller design focuses on the disturbance rejection for low frequencies in order to achieve a good rejection of the in Chapter 2.1. discussed vibrations.
Figure 4.14 shows the intended structure of the deflection feedback control. The considered plant consists of current controller, voice coil actuator, vertical flexures and the moved mass of the scan head. The feeback controller is designed for the plant using the cantilever as sensor. The proportional integral current controller has a cut-off

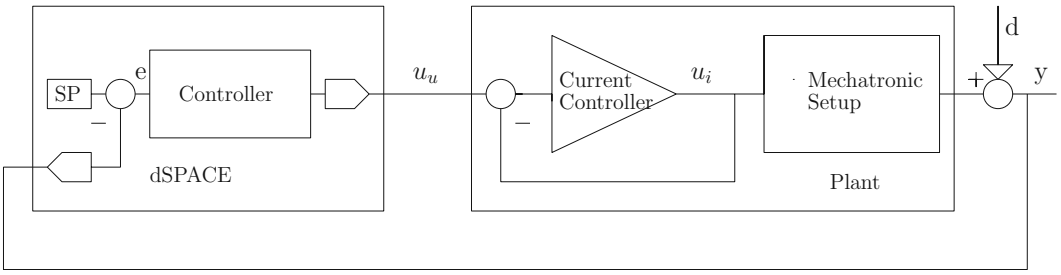

Figure 4.14: Proposed feedback control structure with the controller implemented via dSPACE with the deflection error e as input , the applied voltage u_u to the plant, the inner current control loop, the mechatronic setup consisting of voice coil actuator, flexures and the moved mass leading to the position output y which is disturbed by the disturbance d. The deflection set point SP is set in dSPACE.

frequency of 20 kHz resulting in a cascade control structure. The inner loop is much faster than the outer loop, 1 kHz bandwidth for the outer loop respectively 20 kHz for the outer loop. Since the inner loop is 20 times faster than the outer loop it is assumed with a frequency response of 1. The current controller leads to a phase delay of few degrees at 1 kHz but this phase is included in the transfer function of the plant which is measured from voltage input of the current controller u_u to the output y measured by the cantilever. The controller is implemented via a dSPACE rapid prototyping system and Simulink. The dSPACE is operated at 20 kSamples/s in real time operation mode, this means all adc-read-outs, calculations, and dac-writes are done within 50 μs, which results in a phase delay of -18 degrees due to the dead time of the digital system at 1 kHz.

In order to prevent the cantilever from breaking due to high motion amplitudes at the first resonance a closed loop system identification [72] is done. A low gain and low bandwidth controller is used and the output y is divided by the applied voltage u_u to obtain an estimate transfer function

$$G(j2\pi f) = \frac{y(j2\pi f)}{u(j2\pi f)} \tag{4.2}$$

and a bode plot of the plant. As the desired closed loop bandwidth is 1 kHz a bode diagram from 1 Hz to at least 10 kHz is favored for control design. This is not possible because at approximately 2.5 kHz the tilt mode is excited. Since the cantilever is not placed perfectly in the middle of the AFM-head it is sensitive to this tilt mode, but the single actuator concept is not capable of compensating this mode. Figure 4.15 shows the frequency response closed loop identification from 1 Hz to 1 kHz. As expected the obtained plant G in blue has a first resonance frequency of 236 Hz as in Figure 4.9.

The frequency response in Figure 4.15 shows a phase of -212 degrees at a frequency of 1 kHz. This might come from higher modes and the dead time of the digital system. At 671 Hz there is a small peak which could be due to the mount of the AFM or the 3D printed AFM head in combination with the cantilever holder. The AFM head is more likely since Figure 4.9 does not show the peak. The combination of the low damped first

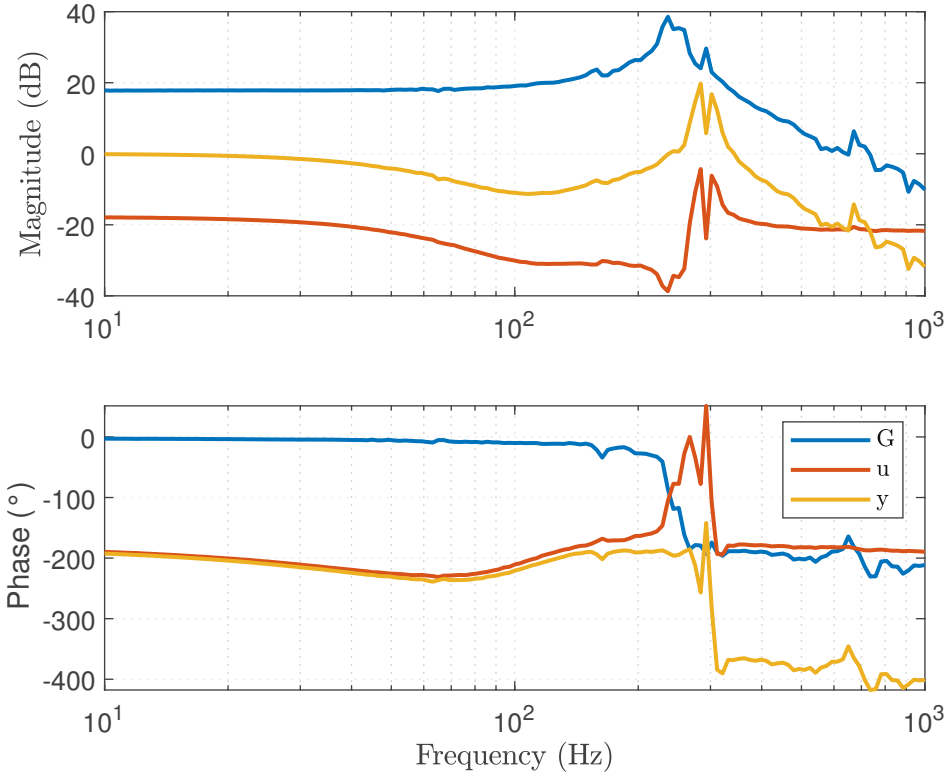

Figure 4.15: Frequency response of the closed loop system identification. The applied voltage u_u is plotted in orange, the position output y is plotted in yellow, and the obtained plant G in shown blue. The first resonance frequency of the system is at 236 Hz as in Figure 4.9.

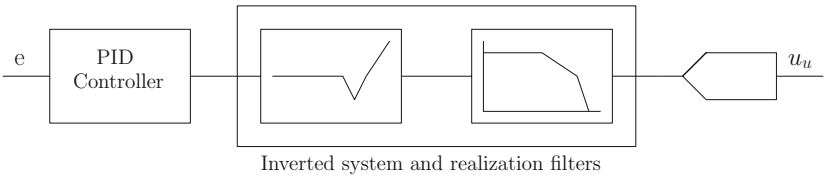

Figure 4.16: Model based control approach, with the PID controller with the deflection error e as input. Before the inverted system with the necessary realization filter.

resonance peak and the high phase delay makes a simple tamed PID control approach impossible.
To enable high bandwidth feedback control the well known part of the mechatronic system is modeled and a model based control approach is used. The idea is outlined in Figure 4.16.The model based approach with PID control is selected because it enables straightforward adjustment of gains to account for variations of the deflection sensitivity. Thus, it enables robust and flexible controller design. Since the stiffness of the milled aluminum flexures is not highly depended on temperature and the moved mass of the AFM head and the moving platform is always constant the used model is a second order system with an experimentally determined damping and a scaling factor. Experiments show that the damping of the first resonance is not depending on the amplitude. This is measured using the additional vertical distance sensor since the high amplitudes at resonance would break the cantilever. The peak at 670 Hz is depending on amplitude and unknown factors and is therefore not modeled. In order to receive a proper system the inverted model is multiplied by two first order filters with a cut-off frequency of 800 Hz and one first order filters with a cut-off frequency of 6000 Hz. This is shown in Figure 4.16. A PID controller is designed for a phase reserve of 60 degrees at 1 kHz for the open loop system. The resulting frequency responses of the controller and the open loop system are shown in Figure 4.17. The phase margin at 1 kHz is as expected 60 degrees and the gain margin of the open loop system is sufficiently high at 6.43 dB. The resulting frequency responses of the closed loop system and the sensitivity function is shown in Figure 4.18.

An alternative would be H-infinity control design which would probably deliver even better disturbance rejection, but every cantilever has a slight difference in sensitivity and the PID controller offers an easy correction by increasing or decreasing the gains without complete redesign of the controller.
The closed loop system is stable and no ringing occurs. The performance of the disturbance rejection is determined in the following chapter The designed controller achieves a disturbance rejection of -40 dB at 5 Hz.

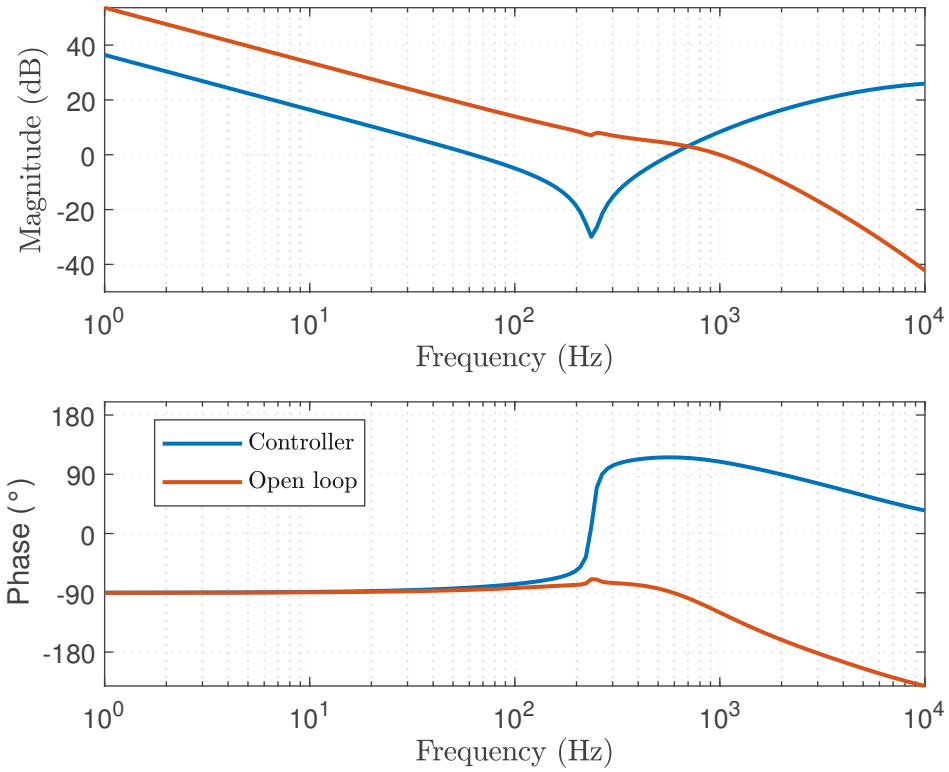

Figure 4.17: The frequency response of the designed controller and the open loop transfer function plotted in blue respectively orange. The controller consists of the PID part, the inverted system and the realization filter. The phase margin at 1 Hkz is 60 degrees and the gain margin is 6.43 dB.

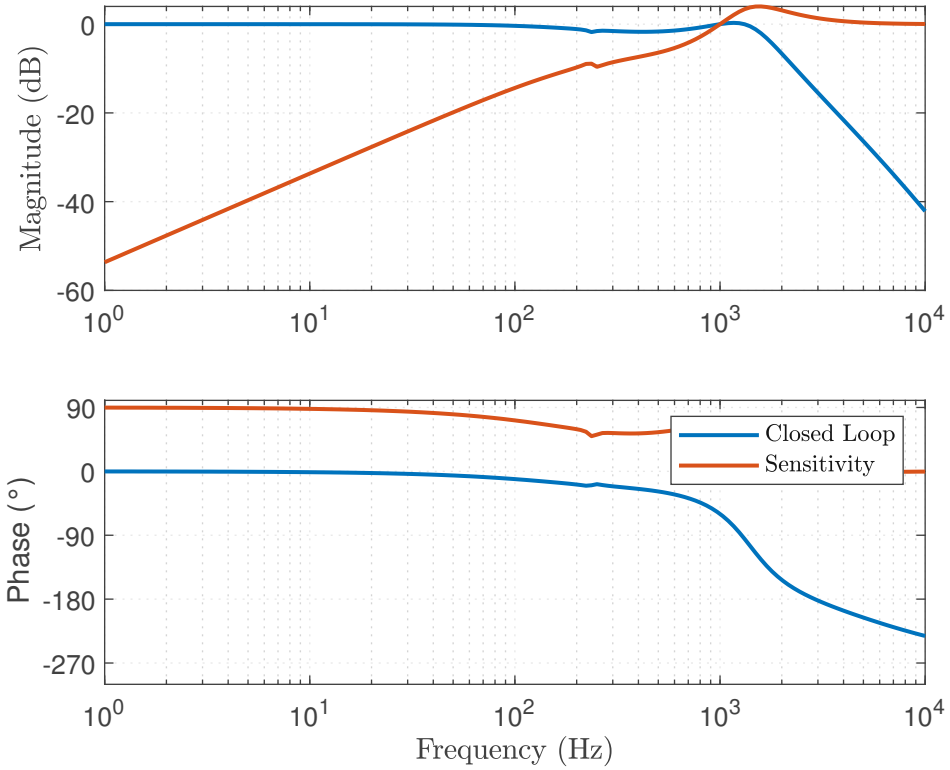

Figure 4.18: The frequency response of the closed loop system with the designed controller and the error sensitivity function plotted in blue respectively orange. The error sensitivity function at 5 Hz is -40 dB.

CHAPTER 5

Experiments with Vibrating Sample

In this chapter the performance of the in Chapter 3.1 proposed methods for topography imaging while the sample is vibrating in-plane respectively out-of-plane is analyzed. The Chapter is finished with an experiment with vibrations simultaneous in-plane and out-of-plane. In order to evaluate the vibration rejection of the controller designed in Chapter 4.6 known vibration profiles are applied to the sample. Sinusoidal disturbances are used to simulate excited structural modes, and band pass filtered white noise simulates floor vibrations with amplitudes and frequencies as suggested in Chapter 2.1. All of the following images are showing the retrace of the AFM images, the trace usually looks similar and is offering no further information. The line scan rate for all images in this chapter is 1 Hz.

5.1 Out-of-plane Vibrations

The cantilever is in contact with the sample and the vertical feedback control keeps the deflection constant. The AFM-head moves in the same way as the out-of-plane vibrations therefore the additional vertical distance sensor just measures a height change if the height of the sample changes during scanning. In this section the out-of-plane vibration rejection is verified with topography measurements of a test grating while the sample is vibrating. The test grating is the same as used in Chapter 4.5. It has 100 nm high squared pits and a pitch of 10 μm. As post processing a plane fit is applied in all images in this section.

5.1.1 Sinusoidal Disturbance with 5Hz and 500nm peak-peak

Figure 5.1(a) shows the uncorrected topography image obtained by the controller output. The sample is vibrating sinusoidal with 500 nm peak-peak and a frequency of 5]Hz out-of-plane during the whole measurement. The disturbance is dominating the topography image. The sinusoidal disturbance is showing up as topography. Figure 5.1 (b) shows

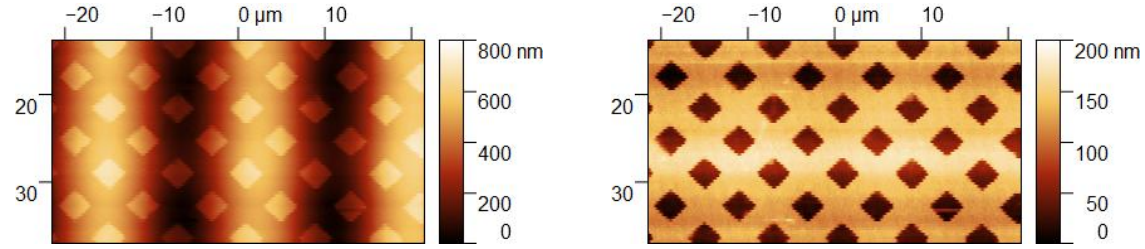

(a) (b)

Figure 5.1: Topography images with a 500 nm peak-peak out-of-plane sinusoidal 5 Hz disturbance, (a) obtained by the uncorrected controller output, (b) corrected topography obtained by the vertical sensor image. The disturbance is not visible in the corrected topography image.

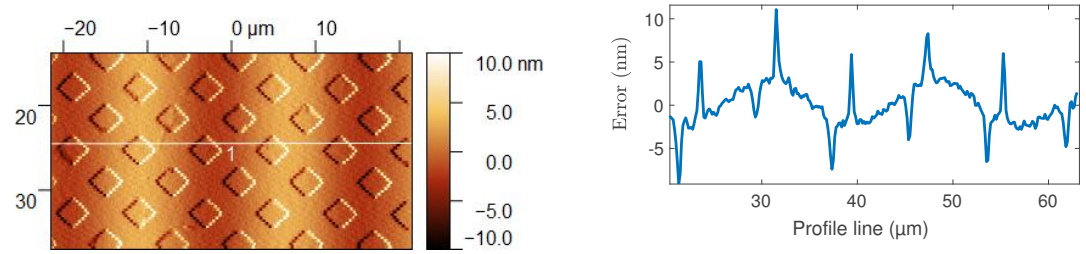

(a) (b)

Figure 5.2: Error analysis with a 500 nm peak-peak out-of-plane sinusoidal 5 Hz disturbance, (a) error image, (b) graph along the line in (a). The graph shows that the remaining sinusoidal error caused by the disturbance is 5 nm peak-peak.

the result of the topography measurement with the additional vertical distance sensor. The topography images have a resolution of 256*128 pixel. In the corrected topography image the disturbance is not visible.
For further analysis a cross section is extracted. The disturbance is still not visible in the cross section. Further insight is provided by the error image in Figure 5.2 (b). The error image shows the error at the controller input during scanning. The edges of the features are typically visible in the error image because a small error occurs before the new sample height is reached. The remaining error due to the sinusoidal disturbance is 5 nm peak-peak and therefore lower than the resolution of the additional vertical distance sensor. A cross section along the profile line in the error image Figure 5.2 (a), is plotted in Figure 5.2 (b). The disturbance rejection S is given by

$$S = 20 \cdot log_{10}(\frac{d_m}{d_a}) = 20 \cdot log_{10}(\frac{5nm}{500nm}) = -40dB, \tag{5.1}$$

where d_m is the measured disturbance and d_a is the applied disturbance. This experiment shows that the out-of-plane disturbance rejection works as intended, with a disturbance rejection of approximately **-40 dB** at 5 Hz, as simulated in Chapter 4.6.

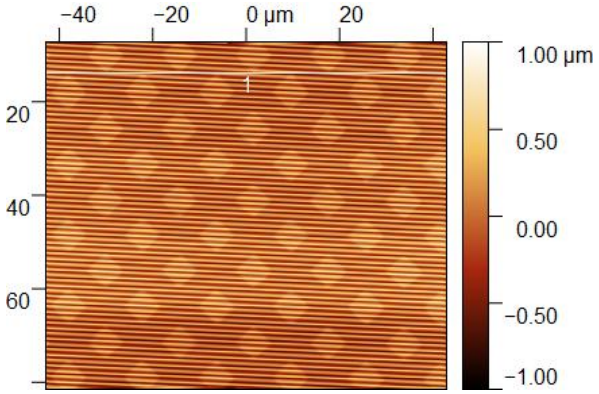

Figure 5.3: Topography image with 1 μm peak-peak out-of-plane sinusoidal 7.3 Hz disturbance obtained by the uncorrected controller output. The disturbance is dominating in the corrected topography image while pits are still visible.

5.1.2 Sinusoidal Disturbance with 7.3Hz and 1um peak-peak

To analyze the influence of higher amplitudes and frequencies a second experiment with sinusoidal vibrations is presented.
Figure 5.3 shows the uncorrected topography image obtained by the vertical controller output. The sample is vibrating sinusoidal with 1 μm peak-peak and a frequency of 7.3 Hz out-of-plane during the whole measurement. The disturbance is dominating the topography image. Figure 5.4 shows the result of the topography measurement with the additional vertical distance sensor. The topography images have a resolution of 262*256 pixel. In the corrected topography image the disturbance is slightly visible.
For further analysis cross sections are extracted and plotted in Figure 5.5. The cross section is along the profile lines as drawn in Figure 5.4 and 5.3. Both profiles are on the same position. Figure 5.6 shows the cross section of the corrected topography image. The selected lines should be a flat surface, but the measured line also includes some edges of the features and noise. Since the rejection of the sinusoidal disturbance is of interest in this section the measured line is filtered to obtain the 7.3 Hz sinusoidal part. The result is shown in Figure 5.5 and zoomed in Figure 5.6 The disturbance rejection S is given by

$$S = 20 \cdot log_{10}(\frac{d_m}{d_a}) = 20 \cdot log_{10}(\frac{16.2nm}{1000nm}) = -38.1dB, \tag{5.2}$$

where d_m is the measured disturbance and d_a is the applied disturbance.
A **-38.1 dB** rejection regarding the sinusoidal disturbance is achieved. The disturbance rejection works with higher amplitudes as well. The simulation of the error sensitivity function in Chapter 4.6 still fits at 7.3 Hz.

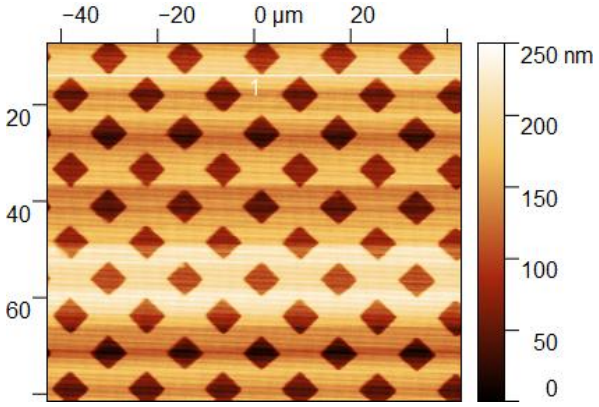

Figure 5.4: Corrected topography images with 1 μm peak peak out-of-plane sinusoidal 7.3 Hz disturbance obtained by the vertical sensor. The disturbance is slightly visible in the corrected topography image.

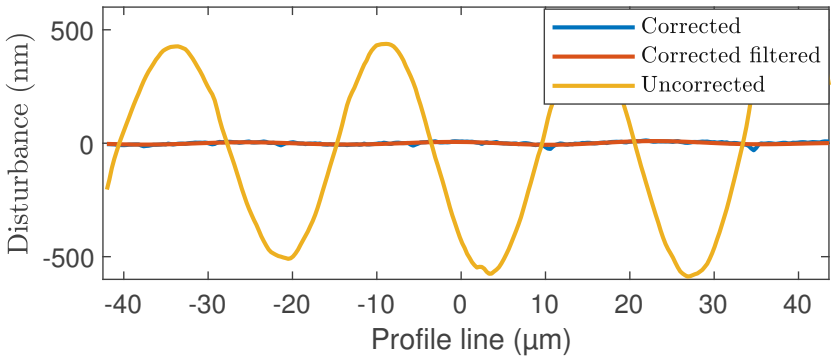

Figure 5.5: Cross section along the profile line as drawn in Figure 5.4 and Figure 5.3. Blue shows the the profile of the corrected topography, orange as well but filtered and yellow shows the profile of the uncorrected topography. The disturbance rejection is well visible in this plot.

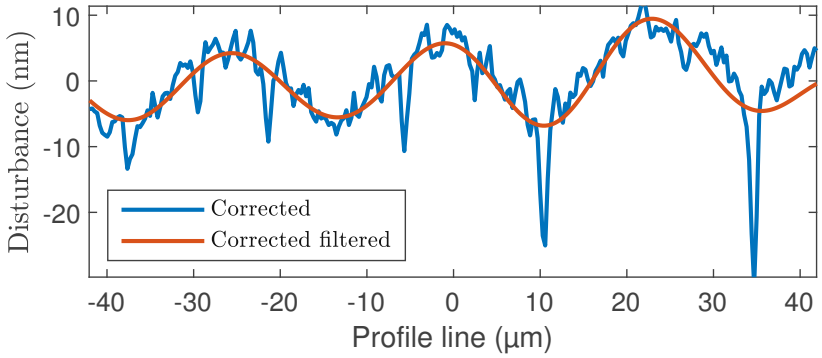

Figure 5.6: Cross section zoom along the profile line drawn in Figure 5.4. Blue shows the the profile of the corrected topography, orange as well but filtered. The peak-peak value due to the disturbance is 16.2 nm.

5.1.3 White Noise with 4um peak-peak

To simulate floor vibrations with high amplitudes filtered white noise is applied to the sample.
Figure 5.7(a) shows the uncorrected topography image obtained by the vertical controller output, the sample is vibrating out-of-plane with a band pass filtered white noise with cut-off frequencies of 1 Hz respectively 15 Hz with 4 μm peak-peak during the whole measurement. The pits are not visible in the topography image. Figure 5.7(b) shows the result of the topography measurement with the additional vertical distance sensor. The pits are well visible in this topography image. The topography images have a resolution of 262*256 pixel. In the corrected topography image the disturbance is slightly visible. For further analysis cross sections are extracted. Along the profile lines in Figure 5.7(a) and (b) the rms is calculated, the mean height was subtracted before. The noise level was reduced from 429 nm_{rms} to 13 nm_{rms}. The disturbance rejection S is given by

$$S = 20 \cdot log_{10}(\frac{d_m}{d_a}) = 20 \cdot log_{10}(\frac{13nm}{429nm}) = -30.3\,dB, \tag{5.3}$$

where d_m is the measured disturbance and d_a is the applied disturbance. A disturbance rejection of **-30.3 dB** is achieved. The disturbance rejection works even with amplitudes which could damage the cantilever without remedies against the vibrations. Topography imaging is still possible although with reduced resolution.

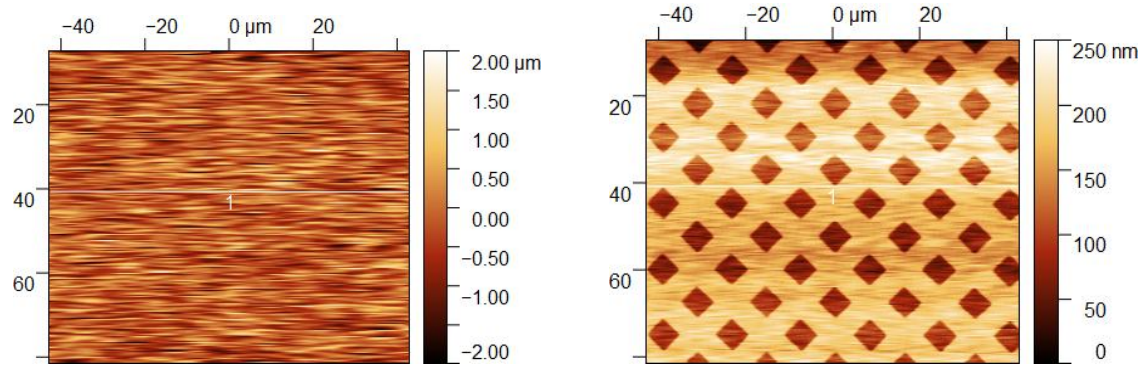

(a) (b)

Figure 5.7: Topography images with $4\,\mu m$ peak-peak Band pass filtered white noise out-of-plane disturbance, Figure (a) shows the the uncorrected topography obtained by controller output, (b) corrected topography obtained by the vertical sensor image. The pits are not visible in the uncorrected topography image. The corrected image clearly shows the pits.

5.2 In-plane Vibrations

In this section the performance of the in-plane correction method is analyzed by several topography measurement experiments. The disturbance to the scan trajectory caused by vibrations is measured and the height values measured at a wrong position are transferred to the positions where they are actually measured in a post processing step.

Since the mouse sensor is not used for topography imaging, the position sensor of the nPoint stage is used as replacement for in-plane distance measurements. Because the time for this thesis does not allow the implementation of an other in-plane measurement system, the in-plane measurement is simulated. The postion sensor output of the nPoint stage has a position noise 0.3 nm. In order to achieve this in-plane resolution in an in-line scenario a sample holder with reflective targets for interferometers has to be designed. The presented experiments should prove the concept.

Vibrations are only applied to the fast axis. Unfortunately the used dSPACE real time rapid prototyping system is not able to run 3-ADCs, vertical feedback controller and moving-average at 20 kSamples/s. Therefore the moving average will be removed for the following experiments and replaced by simple down sampling which is necessary because otherwise memory allocation for the recording of the essential 5-channels will fail. This necessary compromise increase the noise level in the resulting images. It also means that disturbances are just measurable on one axis. Therefore, in-plane vibrations are applied to the fast axis only. A plane fit is applied to all images. All images in this section are taken with line scan rate of 1]Hz and consist of 128 lines and have a resolution of 128 x 128 pixels. The vertical color scale is 0-250 nm for all images. Figure 5.8 shows a reference image. For comparison a reference image is taken and all following images are taken on the same spot.

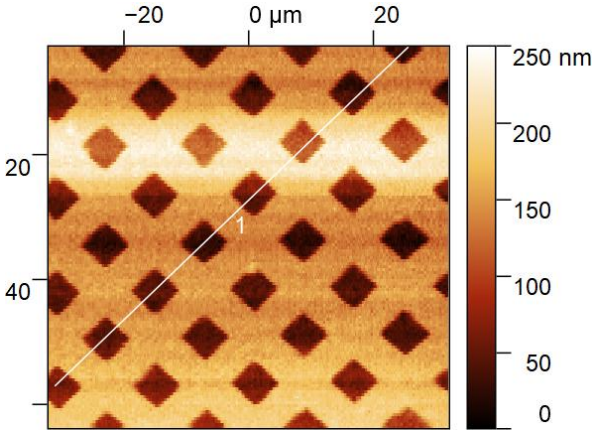

Figure 5.8: Reference spot in-plane vibrations, 1. represents the profile of the extracted reference cross section.

5.2.1 Sinusoidal Disturbance with 1.5Hz and 1um peak-peak

Figure 5.9 (a) shows a topography image of the sample which is vibrating sinusoidal with 1.5 μm peak-peak and a frequency of 1.5 Hz in-plane during the whole measurement. Figure 5.9 (b) shows the result of the applied in-plane correction by disturbance measurement. While the uncorrected image shows frays with the length of the disturbance, the corrected image shows nearly perfect sharp edges. The proposed in-plane correction method works.

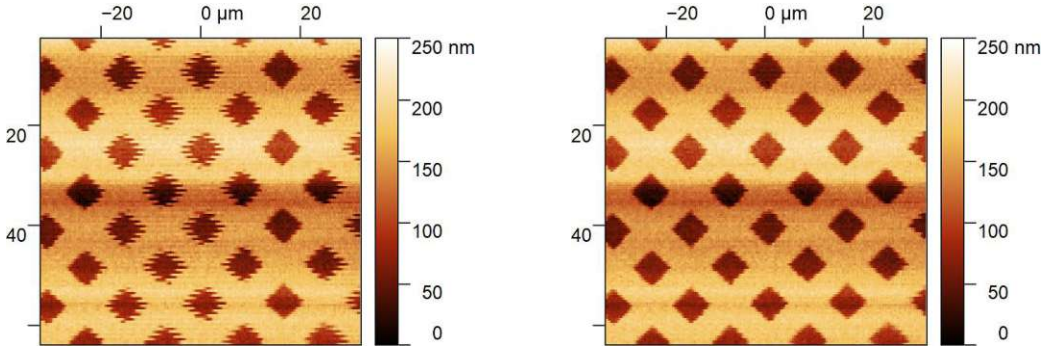

(a) (b)

Figure 5.9: Topography images with a sinusoidal in-plane disturbance with 1.5 μm peak-peak and a frequency of 1.5 Hz. Figure (a) shows the uncorrected topography image. Figure (b) shows the corrected topography image. The corrected image has sharp edges while the uncorrected image shows frays.

5.2.2 Sinusoidal Disturbance with 1.5Hz and 4um peak-peak

To analyze the influence of higher disturbance amplitudes the amplitude of the sinusoidal disturbance is increased to 2 μm. Figure 5.10 (a) shows a topography image of the sample which is vibrating sinusoidal with 4 μm peak-peak and a frequency of 1.5 Hz in-plane during the whole measurement. Figure 5.10 (b) shows the result of the applied in-plane correction by disturbance measurement. While the uncorrected image Figure 5.10 (a) shows frays with the length of the disturbance, the corrected image Figure 5.10 (b) shows no frays anymore but the edges of the features do not have sharp edges anymore. For further analysis a cross section is extracted. The cross section along the profile lines in Figure 5.10 is plotted in Figure 5.11. The uncorrected cross section shows 100 nm high spikes around the pits while the corrected cross section shows nearly rectangular pits and no spikes. The in-plane correction still works with higher amplitudes, but the resolution is declining.

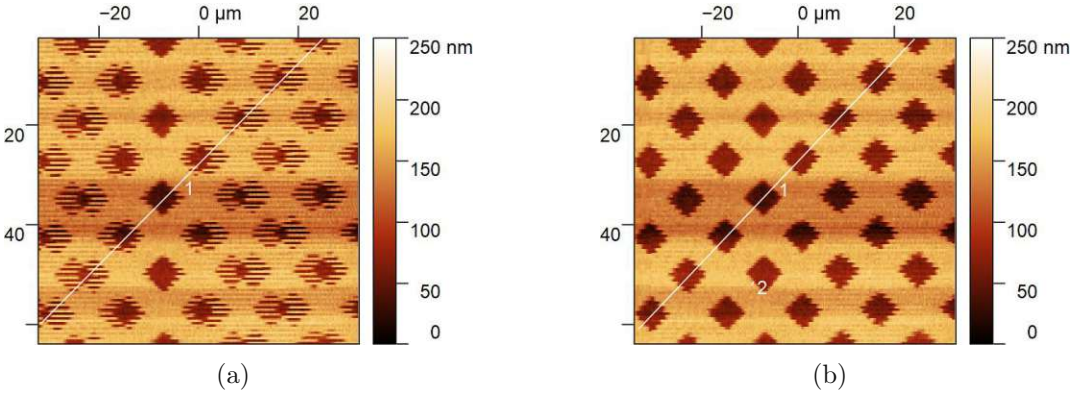

(a) (b)

Figure 5.10: Topography images with a sinusoidal in-plane disturbance with 4 μm peak-peak and a frequency of 1.5 Hz. Figure (a) shows the uncorrected topography image. Figure (b) shows the corrected topography image. The corrected image does not frays, while the uncorrected image shows frays.

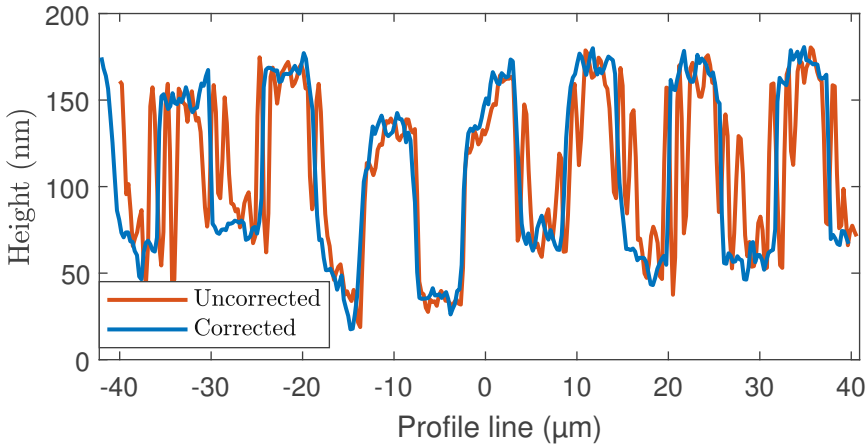

Figure 5.11: Cross section extracted from the line 1. in Figure 5.10. The orange plot shows the uncorrected profile. Blue shows the cross section of the corrected topography. The corrected cross section shows 100 nm high pits as expected.

5.2.3 Sinusoidal Disturbance with 15Hz and 1um peak-peak

To analyze the influence of higher disturbance frequencies the frequency of the sinusoidal disturbance is increased to 15 Hz. Figure 5.12 (a) shows a topography image of the sample which is vibrating sinusoidal with 1 μm peak-peak and a frequency of 15 Hz in-plane during the whole measurement. The topography image does not shows 15 Hz frays because the image resolution is to low to show the 15 Hz frays but the squared pits show a distorted shape. Figure 5.12 (b) shows the result of the applied in-plane correction by disturbance measurement. Figure 5.12 (b) shows squares without disturbances. The in-plane correction still delivers good result with higher frequencies.

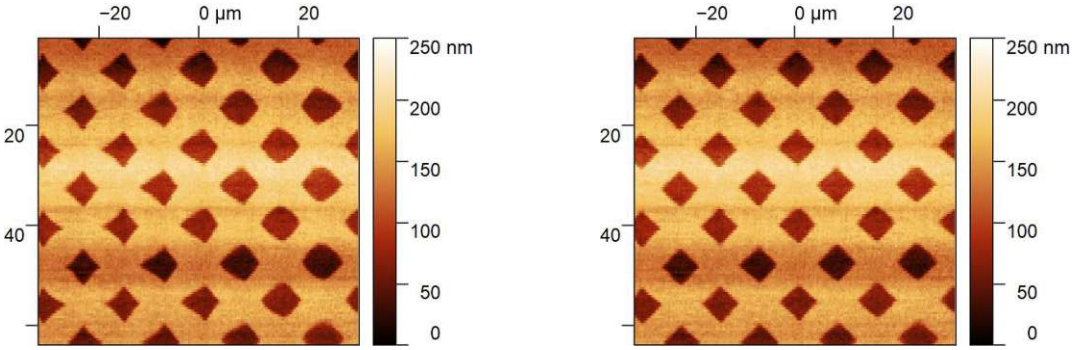

(a) (b)

Figure 5.12: Topography images with a sinusoidal in-plane disturbance with 1 μm peak-peak and a frequency of 15 Hz. Figure (a) shows the uncorrected topography image. Figure (b) shows the corrected topography image. The uncorrected image shows distorted pit shapes while the corrected images shows squares.

5.3 Vibrations In-plane and Out-of-plane

In this section it is analyzed if the out-of-plane compensation and the in-plane correction method can work simultaneously.
The sample is vibrating out-of-plane and in-plane with a band pass filtered white noise with cut-off frequencies of 1 Hz respectively 15 Hz with 1 μm peak-peak during the whole measurement. Figure 5.13 shows the topography image obtained feedback controller output, in this image the topography of the sample is not visible anymore due to vibrations. In Figure 5.14 the topography image obtained by the additional vertical distance sensor is shown. Here are the pits well visible but the edges of the features are not sharp due to the in-plane disturbances, as in Chapter 5.2. After the subtraction of the position error from the planned scan trajectory the edges become sharp, which is well visible by comparing 5.14 with Figure 5.15. As comparison the reference image from Section 5.2 is taken since this experiment is done on the same spot and the same signal processing setup. For further insight the noise along the profile lines in Figure 5.8, Figure 5.13 and Figure 5.15 is extracted but with matching line fit since ac-rms of and the oscillating drift of the strain gauges would make the comparison unfair. In order make a quantitative comparison a profile along an a flat line is selected. The profiles are extracted and their mean value is subtracted, since only the alternating part is of relevance. The result is shown in Figure 5.16. It can be seen that the disturbance rejection works well. For further analysis of the remaining noise the rms of the lines is calculated and compared. Results are shown in Table 5.1

Table 5.1: RMS and peak-peak noise

	rms (nm)	peak-peak (nm)
corrected	11.3	69.8
uncorrected	179.2	1048.3
reference	5.7	30.4

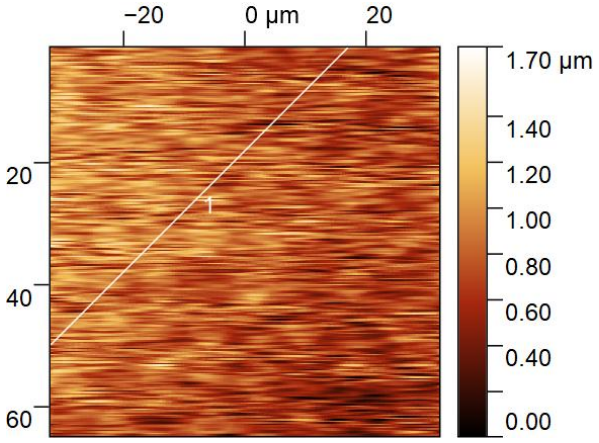

Figure 5.13: Uncorrected topography image with 1 μm peak-peak band pass filtered white noise on both axes obtained by the controller output. The pits are not visible in the uncorrected topography image.

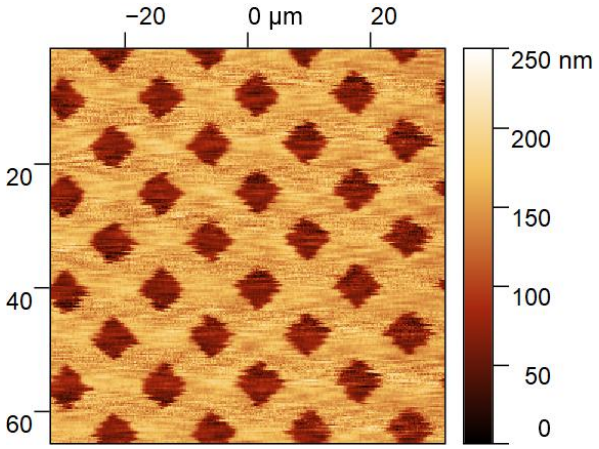

Figure 5.14: Out-of plane corrected topography image image with 1 μm peak-peak band pass filtered white noise on both axes obtained by the additional vertical sensor. The corrected image clearly shows the pits, but the edges of the features are not sharp.

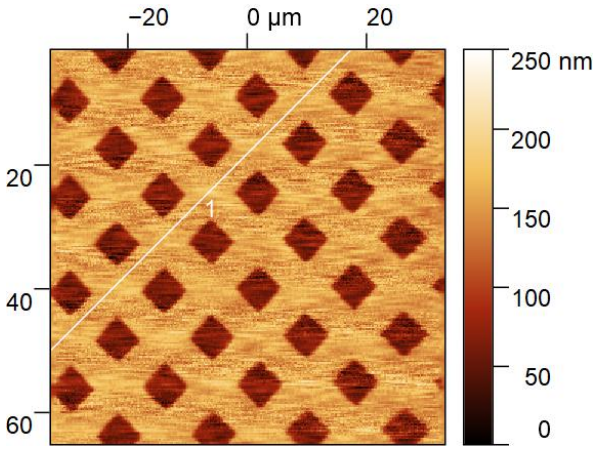

Figure 5.15: Corrected topography image image with 1 μm peak peak band pass filtered white noise on both axes obtained by the additional vertical sensor with in-plane correction applied. The edges of features in this image are sharp.

With the values of Table 5.1 a **disturbance rejection of -24.04 dB** regarding rms noise is achieved, respectively -23.54 dB regarding peak-peak rejection. And the experiment with a vibrating sample only doubled the rms noise compared to the reference measurement without vibrations. Here is to mention that the line fit causes artifacts, but without the comparison is not possible.
However the experiment shows that both in-plane and out-of-plane correction methods can be applied simultaneous and enable AFM topography imaging on samples vibrating in arbitrary direction. All presented experiments in this chapter and many more are performed with the same cantilever. The experiments showed that even though the tip is exposed to high vibrations during the topography measurement the tip is not damaged.

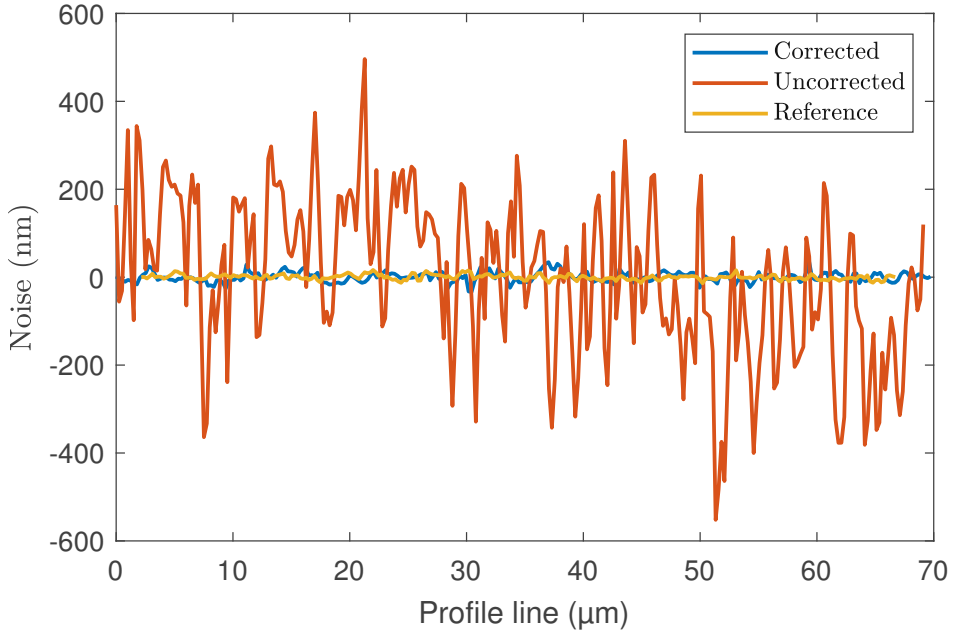

Figure 5.16: Cross section along profile line 1. in Figure 5.15 in blue. Blue shows the cross section of the corrected topography. Cross section along profile line 1. in Figure 5.13 in orange. The orange plot shows the cross section of the uncorrected topography. Yellow show the cross section along the same line in the reference topography image 5.8 with a line fit applied. All profile lines are on the same position. The graph shows a good disturbance rejection.

CHAPTER 6

Long Range Experiments

In this chapter the setups ability to perform long range measurements is analyzed. In in-line measurement scenarios the sample is not always placed perfectly perpendicular to the vertical axis this results in a sample tilt which has to be compensated by the vertical axis. The sample is placed with an approximately 10% slope in the following experiments.Images with a line scan rates of 0.5 Hz and 1 Hz are taken. Long range topography measurements are performed on the same test grating as used in Chapter 4.5. The topography images in this section are obtained by the vertical controller output.

6.1 Line Scan Rate 0.5Hz

Figure 6.1 shows the unprocessed topography image. The sample tilt and the scanner bow are dominating the colour scale. The 100 nm pits are barely visible. Figure 6.2 shows

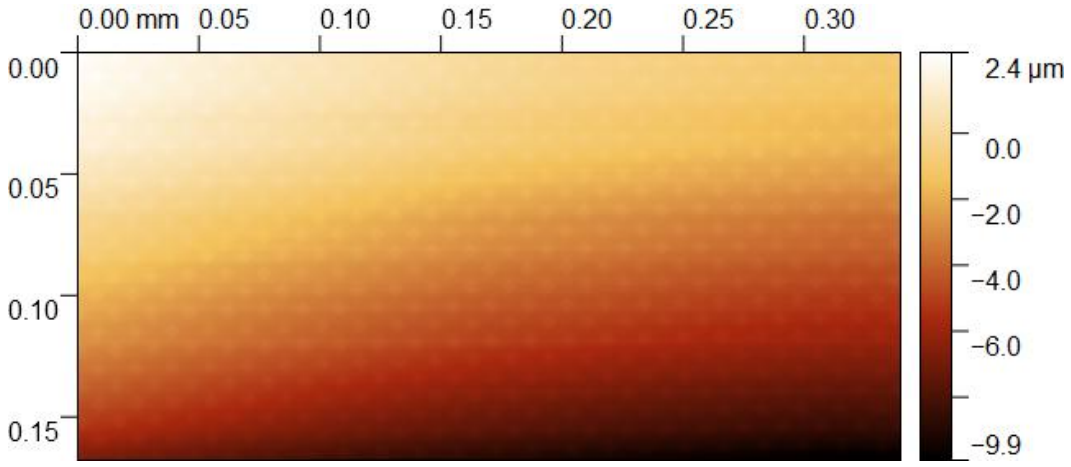

Figure 6.1: Topography image with 340 x 170 μm unprocessed

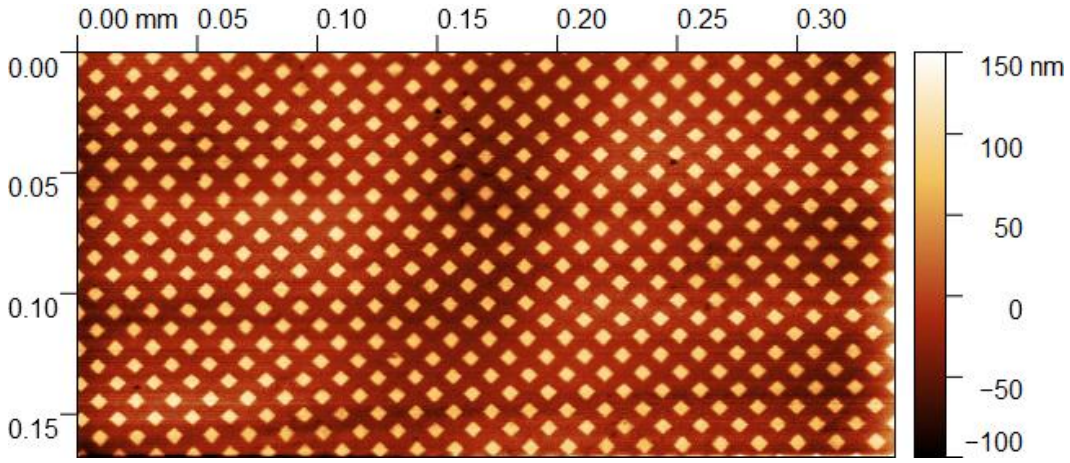

Figure 6.2: Topography image with 340x170μm post processing applied. A polynomial background is subtracted and a line fit is applied. The image has a resolution of 500x247 pixel. The scanner shows high linearity

the post processed topography image. As post processing a polynomial background with coefficients presented in Equation 6.2 is subtracted from the topography image, a plane fit would not compensate the vertical error due to the scanner bow. With a range of 340 μm the scanner bow of the fast axis is 240 nm and already higher than the pits. The vertical error Sb_v due the scanner bow is given as

$$Sb_v = l_f - \sqrt{l_f^2 - (0.5 * r)^2}, \tag{6.1}$$

where l_f is the scanner flexure length and r is the scan range.

$$\begin{aligned} a[0,0] = 2,4899\mu m,\ a[1,0] = -11,866\ 10^{-3},\ a[2,0] = -41,746m^{-1}, \\ a[0,1] = -0,033185,\ a[1,1] = -11,945m^{-1},\ a[2,1] = 21306m^{-2}, \\ a[0,2] = 80,887m^{-1},\ a[1,2] = -4288,1m^{-2},\ a[2,2] = 79,405\ 10^{6}m^{-3} \end{aligned} \tag{6.2}$$

After the subtraction a vertical modus line fit is applied to reject the drift of the piezoresistiv elements. There are no strong non linearities visible. The measured pits are square and the edges are as sharp as the resolution allows, well visible in the zoomed topography image, Figure 6.3. The scan range on the slow axis is limited due to lack of applied voltage for the vertical axis, necessary to compensate the heavy sample tilt. The scanner shows a high linearity over the whole range. The setup is capable of scanning 340 μm at a line scan rate of 0.5Hz.

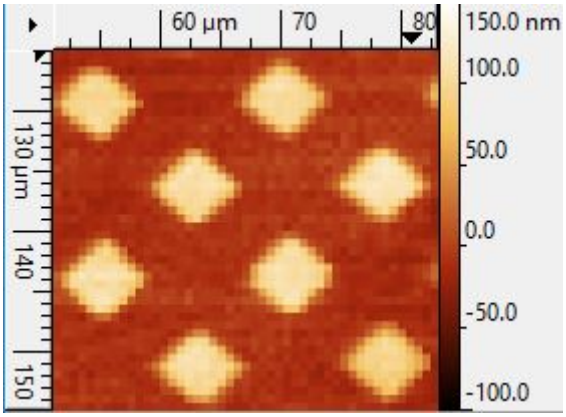

Figure 6.3: Zoomed section from Figure 6.2 the features are still squares with sharp edges.

6.2 Line Scan Rate 1Hz

Figure 6.4 shows the unprocessed topography image. The sample tilt and the scanner bow are again dominating the colour scale. The pits are barely visible. Figure 6.5 shows the post processed topography image. The same post processing was done as in the section before, except with different polynomial coefficients Equation 6.3. In Figure 6.5 a diagonal line is drawn which starts and end in the middle of the two outermost pits, in the middle pit the line is approximately 1 μm of the center. This means the linearity error is less than 0.5%.

$$\begin{aligned} a[0,0] &= 1,2248\mu m,\ a[1,0] = -5,6273\ 10^{-3},\ a[2,0] = -125,27m^{-1}, \\ a[0,1] &= -10,958\ 10^{-3},\ a[1,1] = -13,314m^{-1},\ a[2,1] = 50980m^{-2}, \\ a[0,2] &= 4,9976m^{-1},\ a[1,2] = 35278m^{-2},\ a[2,2] = -58,311\ 10^{6}m^{-3} \end{aligned} \tag{6.3}$$

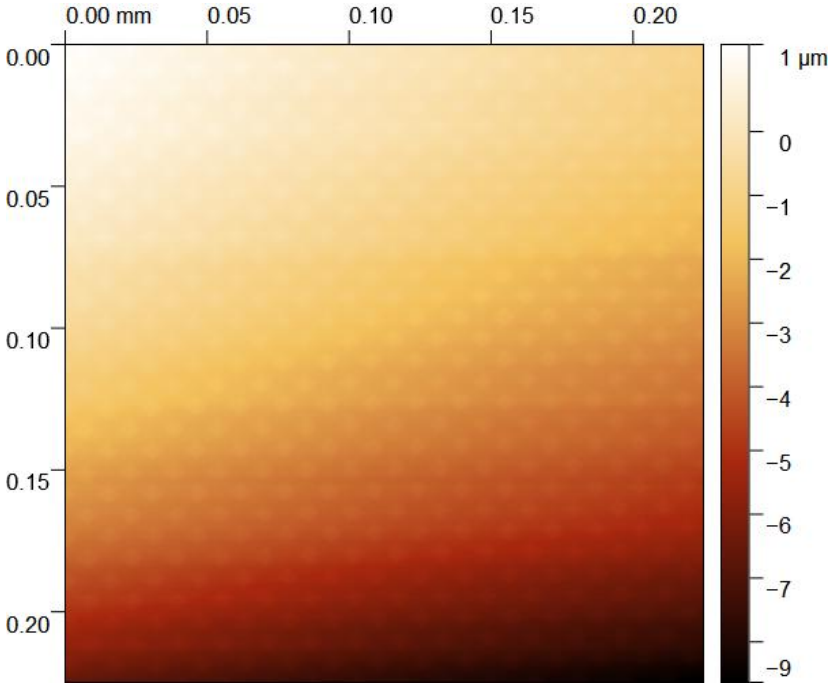

Figure 6.4: Topography image with 225 x 225 μm retrace unprocessed

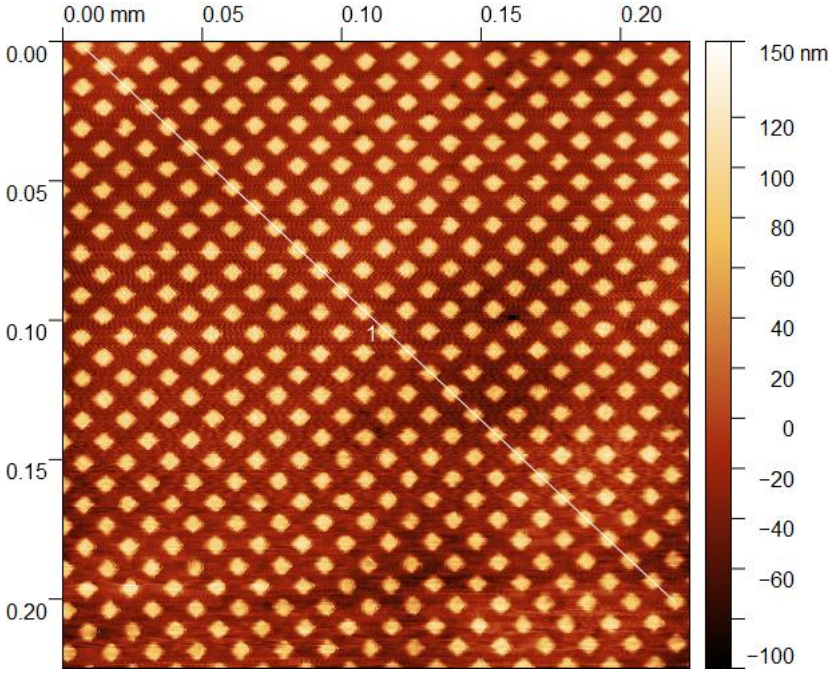

Figure 6.5: Topography image with 225x225 μm with polynomial background subtracted and applied line fit. The scanner shows a high linearity. Line 1 line is drawn which starts and ends in the middle of the two outermost pits. In the middle pit the line is 1 μm of the center which is less than 0.5% linearity error.

CHAPTER 7

Conclusion

With growing demand for products fabricated in the nanoscale the necessity of in-line measurement tool with high resolution arises. The AFM is one of the most versatile measuring tools at the nanoscale. But AFMs are senstive to vibrations and vibrations are omnipresent in industrial environments. Therefore typical vibrations profiles in industrial environments are analyzed and typical remedies against vibrations are discussed. Related work regarding active vibration rejection on AFMs is studied and presented.

Based on this research a concept for an in-line AFM is presented. The out-of-plane vibrations are rejected by feedback control and the topography is obtained by an additional distance sensor. The disturbance to the in-plane scan trajectory is measured during scanning and subtracted in a post processing step. Based on the concept and further requirements for in-line measurement suitable sensors and actuators are selected. The AFM is designed to carry the the selected sensors and meet the requirements defined in Chapter 3.2. The designed parts are milled out of aluminum and the AFM is assembled and evaluated by experiments in Chapter 4.

A flexible and compact AFM with piezoresistive deflection measurement is designed, simulated and evaluated. The AFM is just 16 x 16 x 12 cm and weighs 1.5 kg. The AFM is capable of scanning 220 x 220 μm at a line scan rate of 1 Hz, respectively 340 x 340 μm at 0.5 Hz while the scanner is operated open loop with a linearty error below 0.5%.

Commercially available laser speckle based mouse sensors are not practicably usable for in-plane corrections for AFM images. Literature suggest that a two-dimensional position sensitive photo-detector would be a good alternative. The most dominant error source in the system is the drift of the piezoresistive elements.

A model based feedback controller for the vertical axis with 1kHz bandwidth is designed and tested. The presented vertical single actuator concept is able to reject a sinusoidal out-of-plane disturbance with 5 Hz and 500 nm peak-peak with a disturbance rejection ratio of 40 dB, this is exactly as simulated in 4.18. Further it is shown that it is possible to take AFM topography images while the sample is exposed to vibrations

that would damage the tip, cantilever or both. This is shown by an experiment with $4\,\mu m$ peak-peak white noise with 1- to 15 Hz, $423\,nm_{rms}$ are reduced to $13\,nm_{rms}$.

In-plane vibrations up to $1.5\,\mu m$ are well corrected by the presented offline trajectory error correction method. Both methods still work if the sample is vibrating in-plane and out-of-plane simultaneously. This is tested with white noise vibrations with $1.5\mu m$ on two axes.

7.1 Outlook

Possible measures to improve the presented system are:

- Replacing the in-plane mouse senor with a two-dimensional position sensitive photo-detector for in-plane measurements. If (sub) nanometer resolution is required on the in-plane axes, the introduction of additional reflective targets combined with interferometers is required.
- Prevent the thermal drift of the piezoresistive deflection measurement elements by either compact housing or heating.
- Implement the signal processing and the feedback control on a more powerful digital system to improve the performance of the disturbance rejection and apply vibrations to both in-plane axes.
- Implement tapping mode AFM imaging to reduce the tip sample interaction forces and improve the in-plane correction performance, this could be done using the mechatronic demodulation from [44, 45] and a small tapping piezo on the AFM head or the heater element of the cantilever.

Bibliography

[1] T. M. Pappenfus, R. J. Chesterfield, C. D. Frisbie, K. R. Mann, J. Casado, J. D. Raff, and L. L. Miller, "A π-stacking terthiophene-based quinodimethane is an n-channel conductor in a thin film transistor," *Journal of the American Chemical Society*, vol. 124, no. 16, pp. 4184–4185, 2002.

[2] T. W. Kelley and C. D. Frisbie, "Gate voltage dependent resistance of a single organic semiconductor grain boundary," *Journal of Physical Chemistry B*, vol. 105, no. 20, pp. 4538–4540, 2001.

[3] F. J. Giessibl, "Atomic resolution of the silicon (111)-(7x7) surface by atomic force microscopy," *Science*, vol. 267, no. 5194, pp. 68–71, 1995.

[4] T. Hugel and M. Seitz, "The study of molecular interactions by AFM force spectroscopy," *Macromolecular Rapid Communications*, vol. 22, no. 13, pp. 989–1016, 2001.

[5] C. M. Chan and L. Li, "Direct observation of the growth of lamellae and spherulites by AFM," *Advances in Polymer Science*, vol. 188, pp. 1–41, 2005.

[6] A. S. Hammood, S. S. Hassan, M. T. Alkhafagy, and H. L. Jaber, "Effect of calcination temperature on characterization of natural hydroxyapatite prepared from carp fish bones," *SN Applied Sciences*, vol. 1, no. 5, pp. 1–12, 2019. [Online]. Available: https://doi.org/10.1007/s42452-019-0396-5

[7] M. do Prado, L. C. de Lima, H. Gusman, and R. A. Simão, "Influence of image acquisition on the evaluation of roughness in biomaterials: Roughness measurements in gutta percha cones using atomic force microscopy," *International Journal of Tomography and Statistics*, vol. 13, no. W10, pp. 89–97, 2010.

[8] X. M. Xu and H. Hu, "Development of non-contact surface roughness measurement in last decades," *2009 International Conference on Measuring Technology and Mechatronics Automation, ICMTMA 2009*, vol. 1, pp. 210–213, 2009.

[9] W. Melitz, J. Shen, A. C. Kummel, and S. Lee, "Kelvin probe force microscopy and its application," *Surface Science Reports*, vol. 66, no. 1, pp. 1–27, 2011. [Online]. Available: http://dx.doi.org/10.1016/j.surfrep.2010.10.001

[10] N. Jalili and K. Laxminarayana, "A review of atomic force microscopy imaging systems: Application to molecular metrology and biological sciences," *Mechatronics*, vol. 14, no. 8, pp. 907–945, 2004.

[11] D. Rugar, H. J. Mamin, P. Guethner, S. E. Lambert, J. E. Stern, I. McFadyen, and T. Yogi, "Magnetic force microscopy: General principles and application to longitudinal recording media," *Journal of Applied Physics*, vol. 68, no. 3, pp. 1169–1183, 1990.

[12] M. J. Doktycz, C. J. Sullivan, P. R. Hoyt, D. A. Pelletier, S. Wu, and D. P. Allison, "AFM imaging of bacteria in liquid media immobilized on gelatin coated mica surfaces," *Ultramicroscopy*, vol. 97, no. 1-4, pp. 209–216, 2003.

[13] L. Nony, R. Bennewitz, O. Pfeiffer, E. Gnecco, A. Baratoff, E. Meyer, T. Eguchi, A. Gourdon, and C. Joachim, "Cu-TBPP and PTCDA molecules on insulating surfaces studied by ultra-high-vacuum non-contact AFM," *Nanotechnology*, vol. 15, no. 2, 2004.

[14] G. Binnig, C. F. Quate, and C. Gerber, "Atomic force microscope," *Physical Review Letters*, vol. 56, no. 9, pp. 930–933, 1986.

[15] A. P. Letters and G. M. Ibm, "Erratum : Novel optical approach to atomic force," *Applied Physics Letters*, vol. 1045, no. JANUARY 1989, pp. 22–25, 2016.

[16] M., Tortonese, H. Yamada, B. R. C., and Q. C. F., "Atomic force microscopy using a piezoresistive cantilever," *TANSDUCERS 91*, vol. 91, no. TANSDUCERS, pp. 2–5, 1991.

[17] P. Markiewicz and M. C. Goh, "Simulation of atomic force microscope tips sample/sample tip reconstruction," *Journal of Vacuum Science & Technology B: Microelectronics and Nanometer Structures Processing, Measurement, and Phenomena*, vol. 13, no. 3, pp. 1115–1118, 1995. [Online]. Available: https://avs.scitation.org/doi/abs/10.1116/1.587913

[18] D. Wertjanz, T. Kern, E. Csencsics, G. Stadler, and G. Schitter, "Compact scanning confocal chromatic sensor enabling precision 3-D measurements," *Applied Optics*, vol. 60, no. 25, p. 7511, 2021.

[19] H. Hao, T. C. Ang, and J. Shen, "Building vibration to traffic-induced ground motion," *Building and Environment*, vol. 36, no. 3, pp. 321–336, 2001.

[20] N. Starostina and P. West, "Part II : Sample Preparation for AFM Particle Characterization," Pacific Nanotechnology, Inc., Tech. Rep., 2006.

[21] B. J. Inkson, *Scanning Electron Microscopy (SEM) and Transmission Electron Microscopy (TEM) for Materials Characterization*. Elsevier Ltd, 2016. [Online]. Available: http://dx.doi.org/10.1016/B978-0-08-100040-3.00002-X

[22] M. G. Attinasi, R. De Stefani, E. Frohm, V. Gunnella, G. Koester, M. Tóth, and A. Melemenidis, "The semiconductor shortage and its implication for euro area trade, production and prices," *Economic Bulletin Boxes*, vol. 4, 2021. [Online]. Available: https://ideas.repec.org/a/ecb/ecbbox/202100046.html

[23] Y. Gorodnichenko, O. Talavera, and N. Vu, "Quality and price setting of high-tech goods," *Economic Modelling*, vol. 98, no. September 2020, pp. 69–85, 2021. [Online]. Available: https://doi.org/10.1016/j.econmod.2021.02.010

[24] Y. Sun, N. B. Agostini, S. Dong, and D. Kaeli, "Summarizing CPU and GPU Design Trends with Product Data," 2019. [Online]. Available: http://arxiv.org/abs/1911.11313

[25] J. Ballestín-Fuertes, J. Muñoz-Cruzado-alba, J. F. Sanz-Osorio, and E. Laporta-Puyal, "Role of wide bandgap materials in power electronics for smart grids applications," *Electronics (Switzerland)*, vol. 10, no. 6, pp. 1–26, 2021.

[26] P. Gorai, R. W. McKinney, N. M. Haegel, A. Zakutayev, and V. Stevanovic, "A computational survey of semiconductors for power electronics," *Energy and Environmental Science*, vol. 12, no. 11, pp. 3338–3347, 2019.

[27] P. R. Schmitt and D. F. Moenning, "ENSURE SUCCESS WITH INLINE-METROLOGY," *Metrology for a Sustainable Development*, no. XVIII IMEKO, pp. 17–22, 2006.

[28] D. Imkamp, J. Berthold, M. Heizmann, K. Kniel, M. Peterek, R. Schmitt, J. Seidler, and K. D. Sommer, "Herausforderungen und Trends in der Fertigungsmesstechnik - Industrie 4.0," *Technisches Messen*, vol. 83, no. 7-8, pp. 417–429, 2016.

[29] Ö. Taga, Z. Kiral, and K. Yaman, "Determination of cutting parameters in end milling operation based on the optical surface roughness measurement," *International Journal of Precision Engineering and Manufacturing*, vol. 17, no. 5, pp. 579–589, 2016.

[30] D. F. Hesser and B. Markert, "Tool wear monitoring of a retrofitted CNC milling machine using artificial neural networks," *Manufacturing Letters*, vol. 19, pp. 1–4, 2019. [Online]. Available: https://doi.org/10.1016/j.mfglet.2018.11.001

[31] A. Keyvani, M. S. Tamer, M. H. van Es, and H. Sadeghian, "Simultaneous AFM nano-patterning and imaging for photomask repair," in *Metrology, Inspection, and Process Control for Microlithography XXX*, M. I. Sanchez, Ed., vol. 9778, International Society for Optics and Photonics. SPIE, 2016, p. 977818. [Online]. Available: https://doi.org/10.1117/12.2219041

[32] G. Schitter and A. Stemmer, "Eliminating mechanical perturbations in scanning probe microscopy," *Nanotechnology*, vol. 13, no. 5, pp. 663–665, 2002.

[33] R. Saathof, M. Thier, R. Hainisch, and G. Schitter, "Integrated system and control design of a one DoF nano-metrology platform," *Mechatronics*, vol. 47, pp. 88–96, 2017. [Online]. Available: https://doi.org/10.1016/j.mechatronics.2017.08.013

[34] S. Ito, S. Unger, and G. Schitter, "Vibration isolator carrying atomic force microscope's head," *Mechatronics*, vol. 44, pp. 32–41, 2017.

[35] M. Crispino and M. D'Apuzzo, "Measurement and prediction of traffic-induced vibrations in a heritage building," *Journal of Sound and Vibration*, vol. 246, no. 2, pp. 319–335, 2001.

[36] G. A. Athanasopoulos and P. C. Pelekis, "Ground vibrations from sheetpile driving in urban environment: Measurements, analysis and effects on buildings and occupants," *Soil Dynamics and Earthquake Engineering*, vol. 19, no. 5, pp. 371–387, 2000.

[37] M. Leonesio, E. Villagrossi, M. Beschi, A. Marini, G. Bianchi, N. Pedrocchi, L. M. Tosatti, V. Grechishnikov, Y. Ilyukhin, and A. Isaev, "Vibration Analysis of Robotic Milling Tasks," *Procedia CIRP*, vol. 67, pp. 262–267, 2018. [Online]. Available: http://dx.doi.org/10.1016/j.procir.2017.12.210

[38] E. Jan, D. Laro, E. Jamie, and A. Walter, "The â€œultimate performanceâ€ in floor vibration isolationt," *Mikroniek*, vol. 1, no. 2, pp. 13–21, 2011.

[39] T. Uhrmann, T. Matthias, M. Wimplinger, J. Burggraf, D. Burgstaller, H. Wiesbauer, and P. Lindner, "Recent progress in thin wafer processing," *2013 IEEE International 3D Systems Integration Conference, 3DIC 2013*, no. ii, 2013.

[40] V. Nguyen, J. Johnson, and S. Melkote, "Active vibration suppression in robotic milling using optimal control," *International Journal of Machine Tools and Manufacture*, vol. 152, no. November 2019, p. 103541, 2020. [Online]. Available: https://doi.org/10.1016/j.ijmachtools.2020.103541

[41] E. Csencsics, S. Ito, J. Schlarp, M. Thier, and G. Schitter, "High performance robot-supported 3D inline metrology," *Elektrotechnik und Informationstechnik*, vol. 135, no. 6, pp. 382–388, 2018. [Online]. Available: http://dx.doi.org/10.1007/s00502-018-0636-1

[42] M. Thier, R. Saathof, A. Sinn, R. Hainisch, and G. Schitter, "Six Degree of Freedom Vibration Isolation Platform for In-Line Nano-Metrology," *IFAC-PapersOnLine*, vol. 49, no. 21, pp. 149–156, 2016. [Online]. Available: http://dx.doi.org/10.1016/j.ifacol.2016.10.534

[43] M. Thier, R. Saathof, E. Csencsics, R. Hainisch, A. Sinn, and G. Schitter, "Entwurf und Regelung eines Positioniersystems für robotergestützte Nanomesstechnik," *At-Automatisierungstechnik*, vol. 63, no. 9, pp. 727–738, 2015.

[44] M. Poik, M. Mayr, T. Hackl, G. Schitter, and S. Member, "Mechatronic Demodulation for Dynamic Atomic Force Microscopy Measurement Modes," *Under review*, 2022.

[45] M. Poik, D. Kohl, M. Mayr, C. Kerschner, and G. Schitter, "A mechatronic lock-in amplifier: Integrating demodulation in sensor electronics for measuring mechanical

oscillations," *IEEE Transactions on Instrumentation and Measurement*, vol. 70, pp. 1–8, 2021.

[46] B. F. Ju, W. Gao, J. Aoki, T. Asai, and S. Kiyono, "Compact AFM system for rapid and large area surface topography measurement," *Journal of the Chinese Society of Mechanical Engineers, Transactions of the Chinese Institute of Engineers, Series C/Chung-Kuo Chi Hsueh Kung Ch'eng Hsuebo Pao*, vol. 27, no. 5, pp. 525–530, 2006.

[47] T. F. Yao, A. Duenner, and M. Cullinan, "In-line metrology of nanoscale features in semiconductor manufacturing systems," *Precision Engineering*, vol. 47, pp. 147–157, 2017. [Online]. Available: http://dx.doi.org/10.1016/j.precisioneng.2016.07.016

[48] C. Werner, P. C. Rosielle, and M. Steinbuch, "Design of a long stroke translation stage for AFM," *International Journal of Machine Tools and Manufacture*, vol. 50, no. 2, pp. 183–190, 2010. [Online]. Available: http://dx.doi.org/10.1016/j.ijmachtools.2009.10.012

[49] G. Schitter, K. J. Åström, B. E. Demartini, P. J. Thurner, K. L. Turner, and P. K. Hansma, "Design and Modeling of a High-Speed AFM-Scanner," *IEEE Transactions on Control Systems Technology*, vol. 15, no. 5, pp. 906–915, 2007.

[50] G. Schitter and M. J. Rost, "Scanning probe microscopy at video-rate," *Materials Today*, vol. 11, no. SUPPL., pp. 40–48, 2008. [Online]. Available: http://dx.doi.org/10.1016/S1369-7021(09)70006-9

[51] S. Ito, M. Poik, J. Schlarp, and G. Schitter, "Atomic Force Microscopy Breaking through the Vertical Range-Bandwidth Tradeoff," *IEEE Transactions on Industrial Electronics*, vol. 68, no. 1, pp. 786–795, 2021.

[52] J. Piot, J. Qian, H. Pirée, G. Kotte, J. Pétry, J. P. Kruth, P. Vanherck, C. Van Haesendonck, and D. Reynaerts, "Design of a sample approach mechanism for a metrological atomic force microscope," *Measurement: Journal of the International Measurement Confederation*, vol. 46, no. 1, pp. 739–746, 2013. [Online]. Available: http://dx.doi.org/10.1016/j.measurement.2012.09.012

[53] H. U. Danzebrink, L. Koenders, G. Wilkening, A. Yacoot, and H. Kunzmann, "Advances in scanning force microscopy for dimensional metrology," *CIRP Annals - Manufacturing Technology*, vol. 55, no. 2, 2006.

[54] S. Ducourtieux and B. Poyet, "Development of a metrological atomic force microscope with minimized Abbe error and differential interferometer-based real-time position control," *Measurement Science and Technology*, vol. 22, no. 9, 2011.

[55] D. Briers, D. D. Duncan, and E. Hirst, "Laser speckle contrast imaging: theoretical and practical limitations," *Journal of Biomedical Optics*, vol. 18, no. 3, pp. 035 001–7, 2013.

[56] H. J. Tiziani, "A study of the use of laser speckle to measure small tilts of optically rough surfaces accurately," *Optics Communications*, vol. 5, no. 4, pp. 271–276, 1972.

[57] E. Csencsics, "Integrated compensation-based laser sensor system for in-plane and out-of-plane target tracking," *Applied Optics*, vol. 59, no. 20, p. 6138, 2020.

[58] S. Damian, D. Wertjanz, and S. Georg, "In-plane displacement measurement with a mouse sensor," *Bachelor Thesis*, 2021.

[59] R. C. Da Silva, H. Boudinov, and R. R. Correia, "Design and development of two-dimensional position sensitive photo-detector," *Microelectronics Journal*, vol. 36, no. 11, pp. 1023–1025, 2005.

[60] C. Hu, X. Wang, and B. Song, "High-performance position-sensitive detector based on the lateral photoelectrical effect of two-dimensional materials," *Light: Science and Applications*, vol. 9, no. 1, 2020. [Online]. Available: http://dx.doi.org/10.1038/s41377-020-0307-y

[61] Q. Zhong, D. Inniss, K. Kjoller, and V. Elings, "Fractured polymer/silica fiber surface studied by tapping mode atomic force microscopy," *Surface Science Letters*, vol. 290, no. 1-2, pp. L688–L692, 1993.

[62] R. García and R. Pérez, *Dynamic atomic force microscopy methods*, 2002, vol. 47, no. 6-8.

[63] Y. Wu and Q. Zou, "Iterative control approach to compensate for both the hysteresis and the dynamics effects of piezo actuators," *IEEE Transactions on Control Systems Technology*, vol. 15, no. 5 SPEC. ISS., pp. 936–944, 2007.

[64] D. Wertjanz, E. Csencsics, and G. Schitter, "Three-DoF Vibration Compensation Platform for Robot-Based Precision Inline Measurements on Free-Form Surfaces," *IEEE Transactions on Industrial Electronics*, vol. 69, no. 1, pp. 613–621, 2022.

[65] A. J. Fleming, "A review of nanometer resolution position sensors: Operation and performance," *Sensors and Actuators, A: Physical*, vol. 190, pp. 106–126, 2013, publisher: Elsevier B.V.

[66] Y. Liu, H. Liu, and Z. Chen, "Post-fire mechanical properties of aluminum alloy 6082-T6," *Construction and Building Materials*, vol. 196, pp. 256–266, 2019. [Online]. Available: https://doi.org/10.1016/j.conbuildmat.2018.10.237

[67] S. P. Salisbury and R. Ben Mrad, "Analytical stiffness estimation for short flexures," *Mechatronics*, vol. 16, no. 7, pp. 399–403, 2006.

[68] S. Awtar, A. H. Slocum, and E. Sevincer, "Characteristics of beam-based flexure modules," *Journal of Mechanical Design, Transactions of the ASME*, vol. 129, no. 6, pp. 625–639, 2007.

[69] F. Gustafsson, "Determining the initial states in forward-backward ltering 1 Introduction," *IEEE Transactions on Signal Processing*, vol. 44, no. 4, pp. 988 – 992, 1996.

[70] D. L. Quam, G. B. Williams, J. R. Agnew, and P. C. Browne, "An Experimental Determination of Human Hand Accuracy with a DataGlove," *Proceedings of the Human Factors Society Annual Meeting*, vol. 33, no. 5, pp. 315–319, 1989. [Online]. Available: https://doi.org/10.1177/154193128903300517

[71] Y. Sun and J. H. Pang, "AFM image reconstruction for deformation measurements by digital image correlation," *Nanotechnology*, vol. 17, no. 4, pp. 933–939, 2006.

[72] P. Van Den Hof, "Closed-loop issues in system identification," *Annual Reviews in Control*, vol. 22, pp. 173–186, 1998.

Appendix A

Hiermit erkläre ich, dass die vorliegende Arbeit gemäß dem Code of Conduct, ins- besondere ohne unzulässige Hilfe Dritter und ohne Benutzung anderer als der angegebenen Hilfsmittel, angefertigt wurde. Die aus anderen Quellen direkt oder indirekt übernommenen Daten und Konzepte sind unter Angabe der Quelle gekennzeichnet. Die Arbeit wurde bisher weder im In- noch im Ausland in gleicher oder in ähnlicher Form in anderen Prüfungsverfahren vorgelegt.